ANNUAL REVIEWS

Annual Review of Nuclear and Particle Science

The Future of Solar Neutrinos

Gabriel D. Orebi Gann,[1,2] Kai Zuber,[3] Daniel Bemmerer,[4] and Aldo Serenelli[5,6,7]

[1]Department of Physics, University of California, Berkeley, Berkeley, California 94720, USA; email: gabrielog@berkeley.edu

[2]Nuclear Science Division, Lawrence Berkeley National Laboratory, Berkeley, California 94549, USA

[3]Institute for Nuclear and Particle Physics, Technische Universität Dresden, 01069 Dresden, Germany

[4]Nuclear Physics Division, Helmholtz-Zentrum Dresden-Rossendorf, 01328 Dresden, Germany

[5]Institute of Space Sciences (ICE-CSIC), 08193 Barcelona, Spain

[6]Institut d'Estudis Espacials de Catalunya (IEEC), 08034 Barcelona, Spain

[7]Max Planck Institute for Astronomy, 69117 Heidelberg, Germany

Annu. Rev. Nucl. Part. Sci. 2021. 71:491–528

First published as a Review in Advance on July 9, 2021

The *Annual Review of Nuclear and Particle Science* is online at nucl.annualreviews.org

https://doi.org/10.1146/annurev-nucl-011921-061243

Keywords

solar neutrino, solar fusion, proton–proton chain, carbon–nitrogen–oxygen cycle, astrophysical *S*-factor, thermonuclear reaction rate

Abstract

In this article we review the current state of the field of solar neutrinos, including flavor oscillations, nonstandard effects, solar models, cross section measurements, and the broad experimental program thus motivated and enabled. We describe the historical discoveries that contributed to current knowledge, and define critical open questions to be addressed in the next decade. We discuss standard solar models, including uncertainties and problems related to the solar composition, and review experimental and model solar neutrino fluxes, including future prospects. We review the state of the art of the nuclear reaction data relevant for solar fusion in the proton–proton chain and carbon–nitrogen–oxygen cycle. Finally, we review the current and future experimental programs that can address outstanding questions in this field.

Contents

1. INTRODUCTION AND HISTORICAL OVERVIEW 492
2. SOLAR MODELS 494
   2.1. Solar Composition and the Solar Abundance Problem 495
   2.2. Uncertainties in Solar Models 498
3. NUCLEAR REACTIONS IN THE SUN 499
   3.1. Reactions Important for Solar Neutrinos 500
   3.2. Nuclear Reactions Affecting the *pp* Chain Solar Neutrinos 501
   3.3. Nuclear Reactions Affecting the CNO Solar Neutrinos 502
   3.4. Recommended Future Work 503
4. SOLAR NEUTRINO FLUXES 503
5. SOLAR NEUTRINO PHYSICS 506
   5.1. Solar Neutrino Flavor Change 506
   5.2. Nonstandard Interactions 509
   5.3. Emission of (Un)known Particles 510
6. DETECTION OF SOLAR NEUTRINOS 510
   6.1. Detection Techniques 511
   6.2. Water Cherenkov Experiments 514
   6.3. Liquid Scintillator Experiments 514
   6.4. Hybrid Optical Neutrino Detectors 516
   6.5. Noble Liquid and Solid-State Experiments 517
   6.6. Prospects 519
7. CONCLUDING REMARKS 520

1. INTRODUCTION AND HISTORICAL OVERVIEW

For over 100 years, our understanding of the Sun and its energy production was based on thermodynamic and geological arguments. The modern era was ushered in by an experimental revolution that started with the discovery of radioactivity and the Rutherford experiment (1). In 1920, Lord Eddington suggested that a fusion process might be sufficient for energy generation in stars. The discovery of the tunnel effect by Gamow led Atkinson and Houtermans to conclude that high-energy protons (based on the interplay of Maxwell–Boltzmann distribution and tunneling effect) and small nuclear charge would be favorable to allow fusion processes. This realization led to two fundamental reaction schemes—the *pp* chain and the CNO (carbon–nitrogen–oxygen) cycle—with a mutual equation (2, 3):

$$4p \rightarrow \alpha + 2\nu_e + 26.73\ \text{MeV}, \qquad 1.$$

where neutrinos carry away a small fraction of the total energy available. Neutrinos are produced by several reactions, each of which gives rise to a characteristic energy distribution (i.e., spectrum). The contributions of different reactions to the solar neutrino spectrum are illustrated in **Figure 1**. All neutrinos produced in these cycles are created in the electron flavor. Observation of these neutrinos can offer insights into both the Sun and neutrino properties. A decades-long campaign has yielded regime-altering results and two Nobel Prizes. Yet a number of mysteries remain.

In the 1940s, Pontecorvo suggested using nuclear transitions for neutrino detection. He proposed the reaction $^{37}\text{Cl} \rightarrow {}^{37}\text{Ar}$ for a radiochemical experiment. The threshold for neutrino

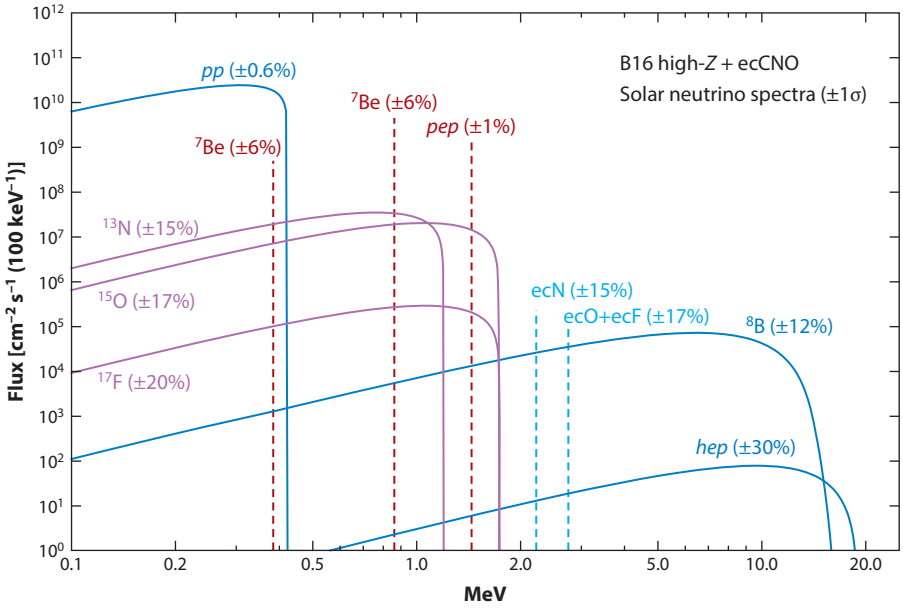

Figure 1

Spectrum of neutrino fluxes from different nuclear reactions (see Section 3). Neutrino fluxes from electron capture (ec) reactions are given in cm^{-2} s^{-1}. Data from Reference 4. Figure adapted from Reference 92.

capture for this reaction is 814 keV. The ^{37}Ar atoms produced in the reaction were collected using small proportional counters to detect the electron capture of ^{37}Ar. Based on the unique physical and chemical properties involved, this proposal developed into the successful Homestake experiment, which resulted in the first observation of solar neutrinos (5, 6). This achievement earned Raymond Davis Jr. the 2002 Nobel Prize in Physics. The experiment surprisingly found a deficit in the solar neutrino flux; only one-third of the expected signal was detected. The energy threshold of the chlorine reaction used in the Homestake experiment meant that it was not sensitive to *pp* neutrinos, which sit very low in the spectrum (**Figure 1**). Access to these *pp* neutrinos was achieved using similar radiochemical techniques in the reaction $^{71}Ga \rightarrow {}^{71}Ge$, which benefits from a *Q*-value of only 233 keV. These measurements, which were performed by the GALLEX Collaboration (7–9) and later the GNO Collaboration (10) in the Italian Laboratori Nazionali del Gran Sasso (LNGS) and by the SAGE Collaboration (11, 12) in the Russian Baksan Neutrino Observatory, all showed deficits in the observed solar neutrino flux.

Around the same time, solar neutrinos were observed by the water Cherenkov experiment Kamiokande (13, 14) via elastic scattering (ES) on electrons. This result confirmed the presence of a deficit with an independent method and achieved the first real-time detection of solar neutrinos. The directional nature of the ES signal was critical in confirming that the observed neutrinos came from the Sun. The experiment was upgraded to Super-Kamiokande (Super-K), a massive detector with a broad physics program that has operated successfully for several decades. The latest solar neutrino results can be found in Reference 15. The threshold for water Cherenkov detection is several MeV, making these experiments sensitive primarily to ^{8}B neutrinos. The detected flux was approximately one-half that expected based on solar models.

LNGS: Laboratori Nazionali del Gran Sasso

This deficit came to be known as the solar neutrino problem, and a clear energy dependence was observed across the different experimental results. Many solutions were proposed with

foundations in astrophysics, nuclear physics, and particle physics. A favorite explanation was neutrino oscillation, the periodic change among the three neutrino flavors. Furthermore, it was recognized that the behavior of neutrinos in matter is modified by the electron density and, in particular, the adiabatic change in electron density to which the neutrino is subjected as it propagates out from the core of the Sun. This change in density causes an additional flavor-changing effect due to the presence of charged current (CC) reactions as well as neutral currents (NCs) for the electron-flavor neutrinos initially produced in fusion reactions (16, 17). The pattern of fluxes across these experiments motivated a new generation of projects that sought to resolve the solar neutrino problem via improved precision, direct detection, and enhanced flavor information.

The Sudbury Neutrino Observatory (SNO) was built to resolve the solar neutrino problem (18, 19). Based on heavy water (D_2O), this experiment offered both an NC reaction and a CC reaction for neutrino detection as well as the ES used in light water Cherenkov detectors. This setup allowed the SNO Collaboration to detect both the pure electron flavor (via CC) and the total flux (via NC) of solar neutrinos, thus demonstrating unequivocally that the measured total solar flux agreed with solar model calculations (20, 21) and that the deficit was due to neutrino flavor change. In 2015, Arthur McDonald and Takaaki Kajita were co-awarded the Nobel Prize in Physics "for the discovery of neutrino oscillations, which shows that neutrinos have mass" (**https://www.nobelprize.org/prizes/physics/2015/press-release/**). Results from SNO remain the only model-independent measurement of the total solar neutrino flux.

The Borexino liquid scintillator (LS) experiment at LNGS (22) was constructed to offer improved spectral precision and sensitivity to lower-energy neutrinos than can be achieved with water detectors. Of particular note is the astonishingly low background achieved in this detector due to unprecedented levels of cleanliness and thermal control. Background radiation typically arises from radioactive contaminants such as the naturally occurring decay chains of ^{238}U and ^{232}Th, ^{14}C, and ^{40}K. By mitigating numerous potential sources of such background, the Borexino Collaboration has been able to complete spectroscopic measurements of all the *pp* chain reactions except the *hep* neutrinos (23, 24) and also has recently provided the first observation of CNO neutrinos (25).

The KamLAND LS experiment in Japan used antineutrinos from nuclear reactors to demonstrate that the observed flavor change was in fact due to oscillation (26). These results, which significantly constrained the parameter space for solar neutrino oscillation, have been the only terrestrial measurement of these parameters.

A number of exciting questions remain in this field. In the remainder of this article, we describe the current status and prospects for advancement. In Section 2, we describe current solar models. In Section 3, we discuss our current understanding of nuclear reactions and cross section measurements needed for future improvements. In Section 4, we present the current best knowledge of solar neutrino fluxes and the dominant uncertainties. In Section 5, we discuss the details of solar neutrino physics, including potential nonstandard effects that could affect oscillation behavior, and in Section 6 we describe the broad experimental program, including multipurpose detectors with sensitivity to solar neutrinos, with an outlook intended to cover the next decade. In Section 7, we conclude with a summary and discussion of future prospects.

2. SOLAR MODELS

Two qualitatively different classes of solar models are used to study solar interior properties: seismic and evolutionary models. Seismic models use helioseismic data, primarily the frequencies of the solar pressure modes (p-modes), to reconstruct the solar internal structure using inversion methods (27–29). They are structural models in that they represent a static picture of the Sun and

do not consider its evolution. This class of models is useful to understand the caveats present in solar models (e.g., missing physical processes) because they reproduce, by construction, the mechanical structure of the Sun. The accuracy and precision of these models are hampered in the innermost solar core ($R \leq 0.1 R_\odot$), the region where most of the ^{7}Be and almost the totality of ^{8}B and CNO neutrinos are produced. Most p-modes do not reach those regions because the internal boundary of their propagation cavity is located outside that region (30, 31). Evolutionary models, the second class of models, follow the evolution of the stellar model from its formation to its present-day age $\tau_\odot = 4.57$ Gyr by integrating spatially and in time the equations of stellar structure and evolution. The minimum requirements imposed on this class of models are that at $\tau_\odot$ the model has $1 M_\odot$ and that it reproduces the solar luminosity $L_\odot$, radius $R_\odot$, and solar surface (photospheric) composition. Evolutionary models are defined by the physical processes included in the equations of stellar evolution. Standard solar models (SSMs) (32–37) include physics that is considered standard in stellar evolution and assume that the Sun has lost a negligible amount of mass during its lifetime. Additional processes, such as dynamical ones induced by rotation, magnetic fields, and gravity waves, can also be included and give rise to nonstandard solar models (non-SSMs) (38–42). Reference 43 provides a recent and very thorough review on SSMs and non-SSMs.

Solar mixture: relative distribution of solar photospheric abundances for all elements heavier than helium (i.e., metals)

2.1. Solar Composition and the Solar Abundance Problem

The chemical composition of the solar photosphere, in particular for elements heavier than helium, is determined with spectroscopic techniques, which require detailed solar atmosphere models, atomic data, and treatment of spectral line formation under nonlocal thermodynamic equilibrium (NLTE) (44–46). Determination of spectroscopic chemical abundances involves a strongly model-dependent procedure, including subjective choices. The abundance of refractory elements can be determined relative to a reference element—typically silicon—from ancient meteorites known as CI carbonaceous chondrites (47). The meteoritic scale can then be placed on the photospheric scale using again one or several refractory elements with reliable photospheric measurements as anchor points (47). The solar mixture is a critical constraint for solar models, and individual elements are relevant as far as they play a significant role in the radiative opacity in the solar interior or in the operation of the CNO cycle (e.g., the primordial solar nitrogen abundance is relevant for the CNO cycle, but its role in the radiative opacity in the solar interior is minor). Solar mixtures are usually characterized by the photospheric total metal to hydrogen mass ratio, $(Z/X)_\odot$, but the detailed abundance pattern is relevant for solar models.

The development of three-dimensional radiation hydrodynamics models, improved atomic data, and NLTE modeling of line formation led to a complete revision of the solar mixture (45). In this review, we refer to these abundances as AGSS09, or low-Z, in the astrophysical nomenclature. Partial revisions with similar techniques are also available (C11) (48). Other hybrid solar mixtures that combine more heterogeneous data sets are also available (47, 49). The largest variations with respect to older solar mixtures (GS98) (50), which predated the aforementioned developments in spectroscopy, occurred for volatile elements, particularly C, N, O, and Ne. In this article, we refer to the solar metallicity from GS98 also as high-Z. A comparison of the solar abundances of the most important elements for solar modeling is presented in **Figure 2** for the GS98, AGSS09, and C11 solar mixtures. Typical uncertainties for each element are in the range 10–12% for volatile elements and <5% for refractory elements. The total photospheric metal to hydrogen ratio is $(Z/X)_\odot = 0.0229$, 0.0178, and 0.0209, respectively, for the three mixtures.

The adoption of a low-Z solar mixture leads to SSMs that do not reproduce the solar internal structure compared with results from helioseismology. This inconsistency is a result of the reduced radiative opacity in solar models with lower metallicity, which is primarily but not only due to the

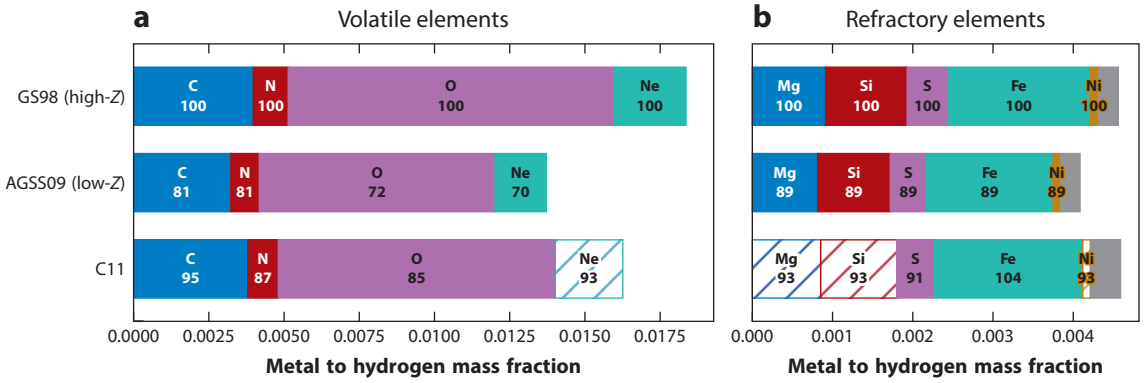

Figure 2

Summary of three different solar mixtures. Photospheric metal to hydrogen mass ratios are shown (*a*) for volatile elements, which constitute most of the solar metallicity, and (*b*) for the most important refractory elements that contribute to the radiative opacity in the solar interior. Note the different scales of the plots. Numbers below element symbols indicate the abundance in percentage of a given element with respect to its GS98 abundance (100% by construction). Hatched areas denote elements not determined by C11 but taken from Reference 49.

reduction in oxygen and neon abundances. The radiative opacity regulates energy transport in the solar interior and, therefore, the mechanical (pressure–density) structure, which solar acoustic oscillations are sensitive to. On the other hand, SSMs that use a high-*Z* solar mixture, although not perfect, reproduce helioseismic results much more satisfactorily (4, 33, 37, 40, 41, 51, 52). This greater reproducibility is best seen in **Figure 3**, which shows the fractional sound speed difference between SSMs with high-*Z* and low-*Z* compositions and the Sun. The discrepancy between low-*Z* solar models and helioseismic inferences on the solar interior—the solar abundance problem—has been the subject of numerous works, starting around 2004 (41, 51, 53–57) and including some comprehensive reviews (43, 58).

Quantifying the disagreement between SSMs and helioseismic and neutrino data is difficult. Several helioseismic diagnostics can be used, such as depth of the convective envelope, surface helium abundance, structural inversion of sound speed, density, and adiabatic index Γ_1 (29, 30, 58). However, correlations among them, and among different regions in the Sun, are not properly quantified in the literature. Moreover, systematic effects related to different methodologies for carrying out helioseismic inversions are not usually addressed (4, 34). The most recent and comprehensive efforts, which rely on sound speed and density inversions and experimental determination of solar neutrino fluxes, yield 0.9σ and 3.0σ agreement levels between model and data for the GS98- and AGSS09-based SSMs, respectively (4, 59, 60).

Solar abundance problem: conflict between state-of-the-art spectroscopic methods and solar structure models; arises because of a 30–40% reduction of the inferred C, N, O, and Ne abundances from novel spectroscopic analysis methods

Several tentative solutions have been put forward to solve the solar abundance problem, both within and outside the framework of SSMs. These include, among others, increased gravitational settling to produce an internal metal-rich and surface metal-poor Sun, increased neon abundance, accretion of metal-poor material from the protoplanetary disk, and solar models with strong mass loss (41, 54, 57, 61–64). No satisfactory solution has been found so far, partly because restoring agreement in a given helioseismic observable sometimes requires modifications in the solar model inputs opposite to those needed to restore agreement in another observable. The most illustrative example is given by the depth of the convective zone and surface helium abundance (56, 65). More contrived models that combine several modifications to solar models have also been proposed (42) and can lead to better agreement, albeit after several ad hoc assumptions. The topic of modified SSMs and non-SSMs has been reviewed extensively in recent literature (43, 46, 66).

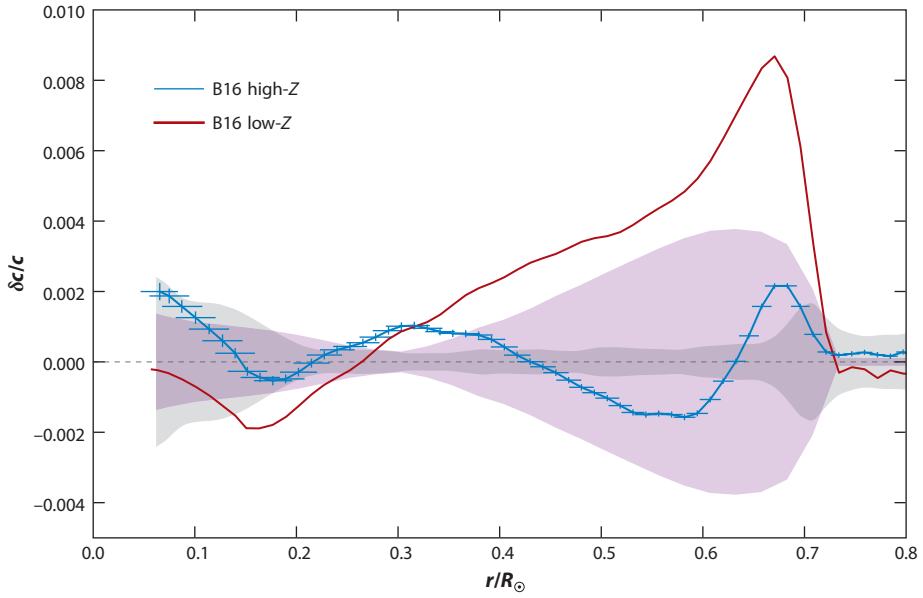

Figure 3

Fractional sound speed difference in the (Sun − model)/model for standard solar models based on high-Z and low-Z solar abundance mixtures. Error bars denote uncertainties due to measurement uncertainties in the solar acoustic oscillation frequencies (*vertical direction*) and size of kernels in the inversion (*horizontal direction*). Shaded areas represent model (*light purple*) and inversion technique (*gray*) 1σ errors. Figure adapted from Reference 4 by permission of The American Astronomical Society.

Modern spectroscopic analysis methods are qualitatively superior to older ones. But the solar abundance problem draws attention to the question of which is the correct photospheric solar composition and, by extension, that of the solar interior. Alternatively, does the current level of disagreement between low-Z SSMs and helioseismology set the best possible accuracy with which SSMs can reproduce the solar internal structure? Independent determinations of the solar metal content are not only desirable but, in fact, fundamental. They hold the key to a detailed understanding of the Sun and all other stars.

The main difficulty in such an independent measurement lies in the fact that metals affect the solar structure only indirectly (e.g., through radiative opacities or the equation of state). Helioseismic diagnostics such as the sound speed profile, depth of convective zone, and surface helium abundance of low-Z SSMs can be made to match helioseismic results by a well-chosen increase in radiative opacities—that is, the degeneracy between metals and atomic opacities is almost complete (52).[1] Alternatively, helioseismic techniques have been used to determine the metallicity of the solar envelope, which should match that of the photosphere. Whereas some works find results consistent with high-Z solar mixtures (67), other, more recent ones have found metallicity values consistent with those of the AGSS09 mixture, and even lower (68, 69). Caution is in order because the helioseismic signal induced by metals is feeble and entangled with that of helium, the results rely on the accuracy of the equation of state, and the systematic uncertainties are difficult to address. On the positive side, such measurements correspond to the adiabatic region of the

[1]Low-Z solar models show a global 3σ disagreement with helioseismic data; high-Z models differ with such data by only 0.9σ.

convective envelope and are therefore independent of the radiative opacities, which are a critical but poorly known input in SSMs (Section 2.2).

2.2. Uncertainties in Solar Models

SSMs establish a well-defined framework in which only three free parameters are adjusted to reproduce the observational constraints: the initial hydrogen and helium abundances and one parameter associated with the treatment of convection. All other physical processes included in non-SSMs require additional free parameters that are tuned either using observational data [e.g., lithium abundance (39), thus removing the model's capability to make testable predictions of this quantity], on hydrodynamic simulations carried out in physical regimes far from those of the solar interior (42), or simply on the best judgment of the researcher [e.g., composition of accreted material (65)]. In this regard, non-SSMs are to some extent phenomenological evolutionary models that are built to explore possible missing physics in SSMs. But quantification of uncertainties is then restricted to SSMs.

Recent work quantifying model uncertainties for neutrino fluxes and helioseismic diagnostics includes References 4, 59, 70, and 71. Uncertainty sources are related either to observational constraints or to the physical inputs (i.e., microphysics) of the models. Among observational constraints, uncertainties in element abundances, in particular from CNO elements, are the major source of uncertainty and dominate the error budget in model uncertainties of helioseismic diagnostics. Reducing the uncertainty in spectroscopic measurements does not seem likely in the near future. Systematic uncertainties, which are hinted at by differences between AGSS09 and C11 values (**Figure 2**), are a reason for concern. They are related to the choice of spectral lines used by the different authors, the underlying solar atmosphere, and the methods of spectroscopic analysis (see, e.g., Reference 72 for an extensive discussion of the solar oxygen abundance determination, which is dominated by systematic uncertainties; see also Reference 73).

Regarding microphysics, radiative opacities remain the most uncertain and critical for solar models. The simultaneously high temperature and density in the solar interior are still not reachable by experiments in a systematic way. Therefore, atomic radiative opacities for solar models rely completely on theoretical calculations. OPAL (74) and OP (75) are widely used sources. The differences between the two have been used as a measure of the uncertainty (59), yielding values from 5% at the base of the convective envelope to 2% in the solar core. The solar abundance problem, however, requires an increase of at least 15% of the opacity at the base of the convective zone from either OPAL or OP to make low-Z SSMs consistent with helioseismic results (41, 52, 53, 59, 60, 76). New atomic opacities (OPLIB) have been presented by the Los Alamos group (77) and by the OPAS Collaboration (78, 79), but differences are similar to those between OP and OPAL except that OPLIB opacities seem too small in the solar core, leading to lower core temperatures and ^{8}B and ^{7}Be neutrino fluxes that are too low to be compatible with experimental results.

The first measurement of radiative opacities at conditions similar to those at the base of the solar convective zone was carried out for iron with the Z machine at Sandia National Laboratories (80). Experimental results yielded larger opacity, by about 40% on the Fe contribution to opacity, than any theoretical calculation. The differences are dominated by a large systematic discrepancy in the quasicontinuum opacity. This result alone implies an increase of 7% in the total opacity of a solar mixture at the base of the convective zone, where Fe is a main contributor (58). The origin of the discrepancy between models and experiment is not yet understood. Further experiments for Cr and Ni were carried out by the same group (81) to enhance understanding. Results point toward problems in theoretical calculations related to, among others, the treatment of line broadening (82–84) and atom–plasma interactions. However, some experimental results

Table 1 Solar neutrino fluxes

Flux	Solar (global)		SSM-B16		Uncertainties		
	No LC	LC	High-Z	Low-Z	Nuclear	Environmental	CNO
$\Phi(pp)$ (10^{10} cm^{-2} s^{-1})	6.21 ± 0.50	$5.971^{+0.037}_{-0.033}$	5.98 (0.6%)	6.03 (0.5%)	0.4%	0.4%	0.1%
$\Phi(pep)$ (10^{8} cm^{-2} s^{-1})	1.51 ± 0.12	1.448 ± 0.013	1.44 (1%)	1.46 (1%)	0.6%	0.8%	0.3%
$\Phi(hep)$ (10^{3} cm^{-2} s^{-1})	19^{+12}_{-9}	19^{+12}_{-9}	7.98 (30%)	8.25 (30%)	30%	1.3%	0.4%
$\Phi(^{7}\text{Be})$ (10^{9} cm^{-2} s^{-1})	4.85 ± 0.19	$4.80^{+0.24}_{-0.22}$	4.93 (6%)	4.50 (6%)	5.0%	4.1%	0.8%
$\Phi(^{8}\text{B})$ (10^{6} cm^{-2} s^{-1})	$5.16^{+0.13}_{-0.09}$	$5.16^{+0.13}_{-0.09}$	5.46 (12%)	4.50 (12%)	7.6%	9.2%	1.9%
$\Phi(^{13}\text{N})$ (10^{8} cm^{-2} s^{-1})	≤13.7	≤13.7	2.78 (15%)	2.04 (14%)	6.2%	6.9%	12%
$\Phi(^{15}\text{O})$ (10^{8} cm^{-2} s^{-1})	≤2.8	≤2.8	2.05 (17%)	1.44 (16%)	8.7%	8.4%	12%
$\Phi(^{17}\text{F})$ (10^{6} cm^{-2} s^{-1})	≤85	≤85	5.29 (20%)	3.26 (18%)	9.3%	9.0%	16%
$\chi 2$			6.0	7.0			

The Solar columns show experimental results with and without the inclusion of the LC. The SSM-B16 columns show results and uncertainties based on GS98 and AGSS09 solar mixtures. The Uncertainties columns show the contributions to model uncertainties from different types of sources. Solar data from Bergström et al. (150). SSM fluxes and uncertainties from Vinyoles et al. (4). Abbreviations: LC, luminosity constraint; SSM, standard solar model.

are still not understood, such as the behavior of the quasicontinuum as a function of the atomic charge of the nucleus in consideration. Overall, the situation regarding radiative opacities is puzzling, and future experimental work is urgently needed (85, 86) along with further development in theoretical calculations (83, 87–90).

Other uncertainty sources related to microphysics are better understood or have a smaller impact on solar model predictions. Uncertainties in the equation of state, however, might have an impact on helioseismic determinations of solar abundances (43, 68, 69). Uncertainties in the gravitational settling rates of heavy elements and helium are estimated to be about 15–20% (91), although this is a rough estimate and relies to some extent on phenomenological constraints such as the surface helium abundance in the Sun. Uncertainties in nuclear reaction rates are discussed in more detail in Section 3.

Uncertainty sources can be grouped according to the way in which they affect solar neutrino predictions: nuclear reactions, which affect individual neutrino fluxes; environmental factors, which affect the solar core temperature; and the abundance of C, N, and O, which directly affects the fluxes in the CNO cycle (for details, see 63, 70, 92).[2] The last three columns in **Table 1** list the total uncertainty for each neutrino flux from each of these three classes; results are taken from Reference 4. Note that metals other than CNO are included as environmental uncertainties because they affect the model neutrino predictions only through their contribution to the radiative opacity in the solar core.

3. NUCLEAR REACTIONS IN THE SUN

In this section, we review the state of the art on nuclear reactions in the Sun and develop recommendations. This text generally follows the approach of the decadal Solar Fusion Cross Sections community meeting–based reviews, here called Solar Fusion I (SFI) and Solar Fusion II (SFII). SFI and SFII include original works up to 1997 (93) and 2009 (94), respectively. A third edition is planned for 2022.

Environmental factor: quantity that affects solar neutrino fluxes through its impact on the thermal structure of the solar core

[2]The composition and opacity represent the main general uncertainty sources for solar models. Nuclear cross section uncertainties matter for specific neutrino fluxes, and opacity calculations disagree with the only available opacity measurement carried out so far under solar conditions.

3.1. Reactions Important for Solar Neutrinos

Astrophysical *S*-factor *S*(*E*): low-energy parameterization of the energy-dependent cross section $\sigma(E)$

Thermonuclear reaction rate: number of nuclear reactions per time and volume

At the temperature of the solar core, only hydrogen burning is relevant, and the *pp* chains dominate (95). For the description of the nuclear reactions inside these chains, the following shorthand notation is adopted here:

$$^3\mathrm{He}(\alpha,\gamma)^7\mathrm{Be} \quad \equiv \quad ^3\mathrm{He} + \alpha \rightarrow \gamma + ^7\mathrm{Be}. \qquad 2.$$

Here, β^+, electron capture, and α decays are denoted as $(e^+\nu_e)$, (e^-, ν_e), and (α).

The three *pp* chains, called *pp*-I, *pp*-II, and *pp*-III, dominate energy production (see **Figure 4*a*** and Section 3.2). The second process of hydrogen burning, the CNO cycle, consists of the CN cycle and the NO cycle and produces the so-called CNO neutrino fluxes (see **Figure 4*b*** and Section 3.3).

For all the nuclear reactions considered here, the Coulomb barrier given by electrostatic repulsion between the two positively charged reaction partners far exceeds the kinetic energy of the thermal motion of the reaction partners in the solar core, even considering the high-energy tails of their thermal Maxwell–Boltzmann distribution. Below the Coulomb barrier, the dependence of the nuclear reaction cross section $\sigma(E)$ on center-of-mass energy E can be parameterized using the so-called astrophysical *S*-factor $S(E)$ (96),

$$\sigma(E) = \frac{1}{E} S(E) \exp\left[-\frac{b}{\sqrt{E}}\right], \qquad 3.$$

with $b = -2\pi Z_1 Z_2 \alpha \sqrt{\mu c^2/2}$ for particles with nuclear charges $Z_{1,2}$, masses $m_{1,2}$, and reduced mass $\mu = m_1 m_2/(m_1 + m_2)$; α is the fine structure constant, and c is the vacuum speed of light. $S(E)$ varies only weakly with energy and encodes the strictly nuclear parts of the cross section. The thermonuclear reaction rate $N_A\langle\sigma v\rangle$ is then given by the product of the *S*-factor (3) and the

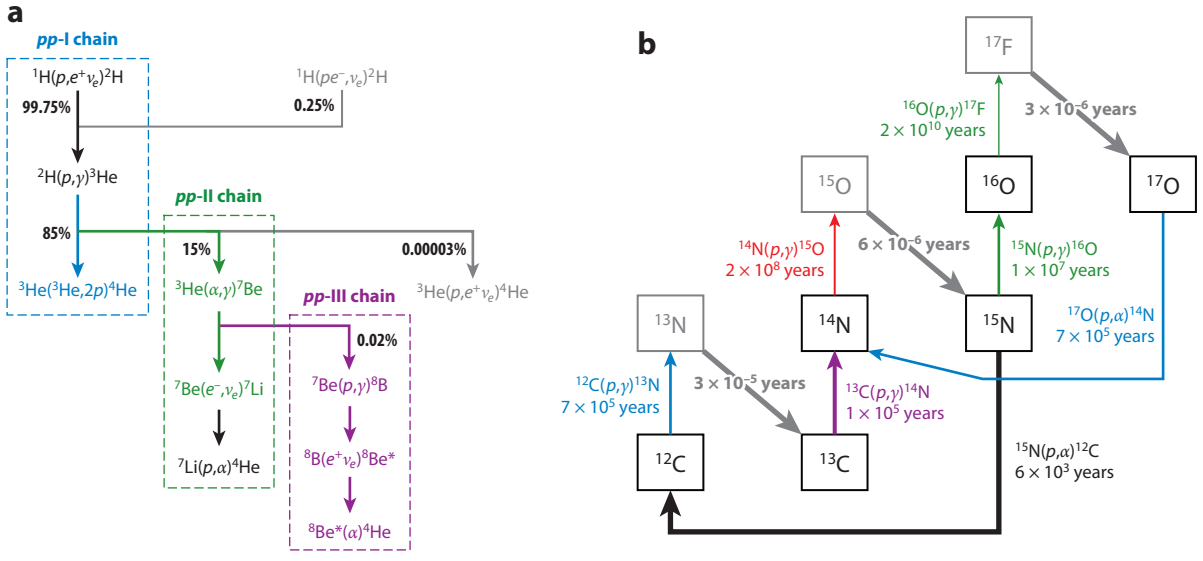

Figure 4

Nuclear reactions in the Sun: (*a*) proton–proton chains and (*b*) the CNO cycle. In panel *b*, effective lifetimes of the starting nuclide against this nuclear reaction ($\tau_{\mathrm{reaction}} = 1/\rho X_{\mathrm{H}} N_A\langle\sigma v\rangle$) or decay ($\tau_{\mathrm{decay}} = 1/\lambda$) are given; ρ is the solar core density, X_{H} is the hydrogen mass fraction, and λ is the decay constant. Wider arrows represent faster transmutations.

Maxwell–Boltzmann distribution for temperature T:

$$N_A\langle\sigma v\rangle = N_A \underbrace{\sqrt{\frac{8}{\mu\pi}}(k_B T)^{\frac{3}{2}}}_{\text{Maxwell}} S(E) \int_0^\infty \exp\left[\underbrace{-\frac{b}{\sqrt{E}}}_{\text{Coulomb}} \underbrace{-\frac{E}{k_B T}}_{\text{Maxwell}}\right] dE. \quad 4.$$

In Equation 4, the energy-dependent factors are labeled with their origins from the Maxwell–Boltzmann distribution or the Coulomb barrier.

The maximum of the integrand of $N_A\langle\sigma v\rangle$ is called the Gamow peak and lies at $E = 6$–28 keV depending on the precise reaction. It is always above the central solar temperature of 1.4 keV but far below the respective Coulomb barrier of 400 to 2,100 keV. As a result, for most nuclear reactions, the cross section is so low that there are no experimental data directly at the energies relevant for solar fusion (i.e., at the Gamow peak). A notable exception is the ^{2}H(p, γ)^{3}He reaction (97, 98). For all other nuclear reactions, experimental data must be taken at the lowest possible energies, including at underground accelerators (99–101), and then extrapolated down to the solar Gamow peak energy.

R-matrix fits provide one possible approach to such extrapolations (102, 103). In R-matrix fits, experimental data from many reaction channels are described in a consistent framework and then extrapolated. This has been attempted, for example, for the ^{14}N(p, γ)^{15}O reaction (94). An alternative approach to derive the low-energy cross section is given by so-called ab initio calculations, which have been reported for *pp* chain reactions such as ^{2}H(p, γ)^{3}He (104) and ^{3}He(α, γ)^{7}Be (105–107).

At the low energies relevant for solar fusion, electron screening (also called electron shielding) reduces the repulsive electric potential of the target nucleus. Electron screening of electrically neutral atoms in the laboratory (108) has to be treated differently than electron screening in the plasma at the center of the Sun (109). Unexpectedly high laboratory electron screening has been reported for some light-ion reactions (110–112). These effects are not strong enough to significantly change the solar fusion reaction cross sections (93, 94, 99, 100), but they are in tension with the general screening framework (109). Experiments at high-power lasers (113), which are essentially screening-free, seem to confirm stellar extrapolations of classical ion beam experiments with standard screening corrections (109). In principle, plasma effects may also affect the rate of nuclear decays, but they are not expected to lead to large deviations (114).

3.2. Nuclear Reactions Affecting the *pp* Chain Solar Neutrinos

The rates of all three *pp* chains, and hence overall energy production and the equilibrium temperature of the Sun, are controlled by the initial reaction, ^{1}H(p, $e^+\nu_e$)^{2}H. Its cross section is many orders of magnitude too low to be accessible experimentally. However, theoretical work has converged to an accepted value with an uncertainty as low as 1% (94), in agreement with more recent calculations on the lattice (115). As indicated by highly precise underground data (97, 98), the subsequent reaction, ^{2}H(p, γ)^{3}He, proceeds much faster and thus does not limit the *pp* chains.

The intersection between the *pp*-I and *pp*-II chains is given by the competition between the ^{3}He(^{3}He,2p)^{4}He (*pp*-I) and ^{3}He(α, γ)^{7}Be (*pp*-II) reactions, which occur in about 83% and 17% of cases, respectively. For the ^{3}He(^{3}He,2p)^{4}He reaction, an LNGS-based cross section measurement at the Laboratory for Underground Nuclear Astrophysics (LUNA) ruled out a previously postulated resonance (116). The ^{3}He(α, γ)^{7}Be reaction has been studied over a wide energy range, but not yet at solar energies (117–120 and references therein). With uncertainties from the extrapolation taken into account, its solar rate is believed to be known with 5% uncertainty, using the

weighted average of all the experiments (94). A further improvement hinges on theoretical (121) and experimental work connecting the well-studied 1-MeV interaction energy range to the solar Gamow peak at ∼0.02 MeV.

CNO cycle: the ensemble of the CN and NO cycles

CN cycle: carbon–nitrogen cycle, which begins and ends at ^{12}C, passing through ^{14,15}N

NO cycle: nitrogen–oxygen cycle, which begins at ^{15}N and returns to ^{14}N; in the Sun, it mainly starts from preexisting ^{16}O

The rate of the third branch, *pp*-III, is much lower (0.00002%) and is given by the competition between the electron capture decay of ^{7}Be (*pp*-II) and the ^{7}Be$(p,\gamma)^{8}$B reaction (*pp*-III). Because of its low cross section and the presence of a strong resonance that complicates the extrapolation, the ^{7}Be$(p,\gamma)^{8}$B reaction is difficult to study in the laboratory. Its accepted rate is 8% precise (94) and is mainly based on an experiment using a proton beam incident on radioactive ^{7}Be targets (122, 123). However, radioactive ^{7}Be beam data hint at a lower cross section (124), so further work may be needed.

Finally, two additional nuclear reactions branch out to and from the three main *pp* chains shown in **Figure 4*a***: ^{1}H$(pe^{-}, \nu_e)^{2}$H (*pep*) is an alternative starting point for all three chains, and ^{3}He$(p, e^{+}\nu_e)^{4}$He (*hep*) is an alternative termination to the *pp*-I chain. Both give rise to low neutrino fluxes, and neither can be studied in the laboratory.

3.3. Nuclear Reactions Affecting the CNO Solar Neutrinos

The CNO cycle (2, 3) (**Figure 4*b***) starts from preexisting ^{12}C in the solar core. In equilibrium, the lifetime of the cycle is dominated by its slowest reaction, ^{14}N$(p,\gamma)^{15}$O. This reaction takes more than 99% of the integrated time of all six transmutations in the cycle, so that almost all the initial ^{12}C is transmuted to ^{14}N and stored there.

Two other nuclear reactions also play interesting roles in CNO burning: ^{12}C$(p,\gamma)^{13}$N and ^{16}O$(p,\gamma)^{17}$F. The temperature dependence of the former is less steep than for the ^{14}N$(p,\gamma)^{15}$O case. As a result, in the early Sun and also in the outer layers of the present-day solar core, this reaction controls the onset of CNO burning, causing a double-peaked structure in the radial emission profile of the ^{13}N neutrinos (95) (see **Figure 6** in Section 4).

The CN and NO cycles intersect at ^{15}N, but the 2,000-fold higher rate of ^{15}N$(p,\alpha)^{12}$C compared with ^{15}N$(p,\gamma)^{16}$O (125, 126) hinders the passage of nucleosynthetic material between these cycles in the Sun. Instead, preexisting ^{16}O feeds the ^{16}O$(p,\gamma)^{17}$F reaction in the Sun. The flux of ^{17}F neutrinos therefore depends on the initial ^{16}O abundance of the Sun and the (very slow) ^{16}O$(p,\gamma)^{17}$F reaction. Any ^{17}F produced is quickly returned to the ^{14}N reservoir by way of the ^{17}O$(p,\alpha)^{14}$N reaction (127).

Because of its paramount importance for the rate of the CN cycle and, hence, the predicted integral flux of ^{13}N and ^{15}O neutrinos, the ^{14}N$(p,\gamma)^{15}$O reaction has been studied many times (128, 129, and references therein; see also **Figure 5**) since it was initially proposed by Bethe (3) and von Weizsäcker (2). The ^{14}N$(p,\gamma)^{15}$O rate was reduced by a factor of two in SFII (94) compared with the rate given in SFI (93). This strong revision was due to an even stronger reduction in the contribution by capture to the ground state of ^{15}O, based on indirect experiment, theory, and direct experiment (130–136).

The latest community-based extrapolated zero-energy *S*-factor, $S_{1,14}(0) = (1.60 \pm 0.09)$ keV·b, was determined using the SFII R-matrix analysis (94) and is corrected here for an updated strength of the normalization resonance (137). Of the two most recent individual studies, one hints at a somewhat higher *S*-factor (128). As a result, here $S_{1,14}(0) = (1.60 \pm 0.13)$ keV·b is recommended (i.e., an error of 8%) so that the recent results are included in 2σ.

The rate of the ^{12}C$(p,\gamma)^{13}$N reaction is more uncertain, at 16% (94, 138). The last comprehensive study of this reaction dates back to 1974 (139).

For ^{16}O$(p,\gamma)^{17}$F, there is an evaluated *S*-factor curve with 6–7% uncertainty at high energy—0.5 to 2.5 MeV in the laboratory (141). At the energies relevant here (the Gamow peak energy), SFII recommends a slightly higher error, 8% (94), based on theory and extrapolations.

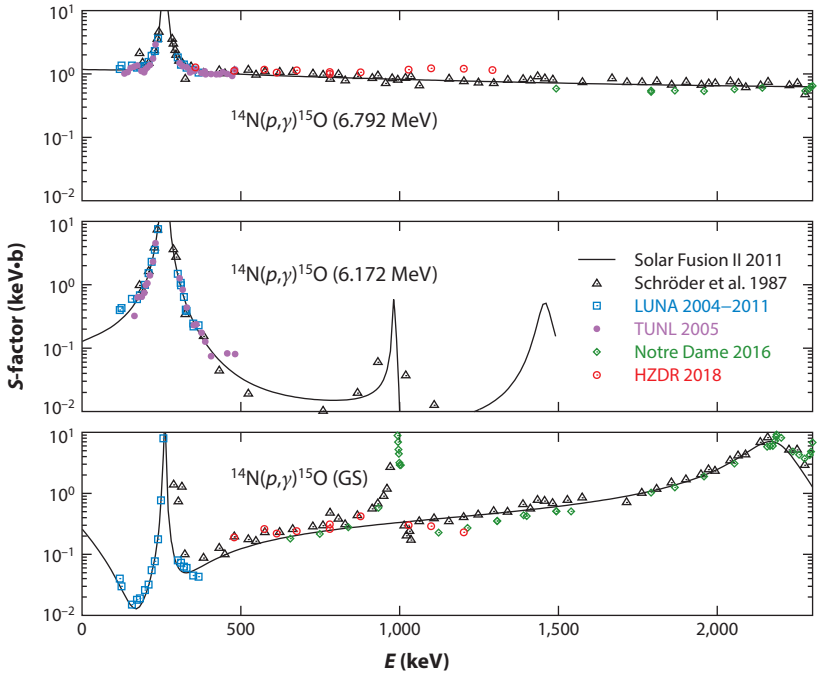

Figure 5

Astrophysical *S*-factor of the ^{14}N(p, γ)^{15}O reaction as a function of center-of-mass energy *E*. The three most important transitions are shown: capture to the ^{15}O excited states at 6.792 MeV (*top*) and 6.172 MeV (*middle*) and to the ground state (*bottom*). Experimental data are from Schröder et al. (140), LUNA (132, 133, 135, 136), TUNL (134), Notre Dame (128), and HZDR (129). The lines are R-matrix fits from Solar Fusion II (94) and precede the latest two experiments (128, 129). Abbreviation: GS, ground state.

Unlike the *pp* chain reactions, no ab initio theoretical description has yet been reported for any of the CNO nuclear reactions, even though this mass range has recently become at least in principle accessible (142).

3.4. Recommended Future Work

New experiments and new theoretical work should go hand-in-hand to improve the precision of the rates of the *pp* chain reactions ^{3}He(α, γ)^{7}Be and ^{7}Be(p, γ)^{8}B to 3%, so as to match the recent ^{2}H(p, γ)^{3}He case (97, 98). For the three key CNO reactions, ^{14}N(p, γ)^{15}O, ^{12}C(p, γ)^{13}N, and ^{16}O(p, γ)^{17}F, new data are needed to bring the precision to 5%. In addition, new theoretical approaches should be extended to address these cases. Finally, new capabilities offered by high-power lasers should be used to study the radiative opacities of C, N, and O and also higher-charge-number atoms in the laboratory as well as plasma effects on nuclear reactions and decays.

4. SOLAR NEUTRINO FLUXES

The theoretical solar neutrino spectrum in **Figure 1** shows the five fluxes associated with the *pp* chain and the continuum fluxes from the β^- decay of ^{13}N, ^{15}O, and ^{17}F in the CNO cycle as well as those from the monoenergetic e^- captures on the same isotopes (143–145). In this review, we denote neutrino fluxes at the Earth as $\Phi(X)$, where X indicates the specific neutrino flux.

Global analyses of solar and terrestrial experimental neutrino data have been used to determine the solar neutrino fluxes (146, 147). In the last decade, the Borexino Collaboration has played a

fundamental role after publishing initial results for the ^{7}Be flux (148), as nicely illustrated first in Reference 149. This work has been updated in Reference 150 by including all experimental neutrino data available up to 2016. These experimental solar neutrino fluxes are reported in **Table 1** as "No LC" (no luminosity constraint).

The energy produced by nuclear reactions in the Sun can be determined from the neutrino fluxes:

$$\frac{L_{\rm nuc}}{(1\,{\rm AU})^2} = \sum_{i=1,8} \alpha_i \Phi(X_i), \qquad 5.$$

where the sum extends over all neutrino fluxes (neglecting fluxes from CNO electron capture; see **Figure 1**), α_i represents the energy contributions of the reactions associated with each of the fluxes (36, 150), and AU is the astronomical unit. Replacing $\Phi(X_i)$ with experimental results, the nuclear energy production in the Sun is

$$L_{\rm nuc} = 1.04^{+0.07}_{-0.08}\, L_\odot. \qquad 6.$$

The uncertainty is dominated by the uncertainty of $\Phi(pp)$. The latter is primarily determined by the contribution of all the gallium experiments to the global analysis and the constraining power of the Borexino results on $\Phi(^7{\rm Be})$.

Equation 6 represents the most accurate and precise experimental determination of the origin of energy in the Sun, a quest that started more than a century ago. The need to further improve this result, in particular reducing the uncertainty, stems from the possibility that nonstandard channels might also be present. This is, for example, the case for axion-like particles (ALPs; see Section 5.3). For some of these particles, such as axions, the most stringent upper limits on energy losses from the Sun come from helioscopes. In other cases, such as dark photons and millicharged particles, limits from solar models offer the most constraining power in regions of parameter space (151, 152). These limits arise from a combination of solar neutrinos and helioseismic probes and establish a maximum energy loss through the nonstandard channels of 1% to 2% of $L_\odot$ to 1σ—much better than the current purely experimental result expressed in Equation 6. But they are model dependent and, to some extent, subject to uncertainties in the accuracy of solar models. A large improvement in the experimental result is highly desirable. For this, a precise measurement of $\Phi(pp)$ is needed. If experimental data are complemented by the solar luminosity constraint (LC) (36, 153), which assumes that the solar luminosity is produced by nuclear reactions, the result is

$$L_{\rm nuc} = 0.991^{+0.005}_{-0.005} + 0.009^{+0.004}_{-0.005}\, L_\odot, \qquad 7.$$

where the first term refers to the energy originating from the *pp* chains and the second one to energy from the CNO cycle. The individual fluxes resulting from this analysis are listed in **Table 1** in the LC column. The largest impact of including the LC occurs for $\Phi(pp)$, which controls most of the energy production in the Sun, and for $\Phi(pep)$, which is directly linked to $\Phi(pp)$ (94, 154).

The Borexino Collaboration has subsequently reported measurements of all the individual reactions in the *pp* chain (23, 24, 155), including a direct measurement of $\Phi(pp) = 6.10 \pm 0.5^{+0.3}_{-0.5} \times 10^{10}$ cm^{-2} s^{-1}, an upper limit of $\Phi(hep) < 2.2 \times 10^5$ cm^{-2} s^{-1} flux, and the most stringent measurement to date of the ^{7}Be flux, $\Phi(^7{\rm Be}) = 4.99 \pm 0.11^{+0.6}_{-0.8} \times 10^9$ cm^{-2} s^{-1} (the quoted uncertainties are statistical and systematic, respectively). Finally, the Borexino Collaboration has also provided the first ever direct measurement of the combined neutrino flux from the CNO cycles (25), $\Phi({\rm CNO}) = \Phi(^{13}{\rm N}) + \Phi(^{15}{\rm O}) = 7^{+3}_{-2} \times 10^8$ cm^{-2} s^{-1}. A comparison with results of the global analysis without the LC (**Table 1**) shows that the Borexino measurement improves on some solar neutrino fluxes. However, a global analysis to determine the solar

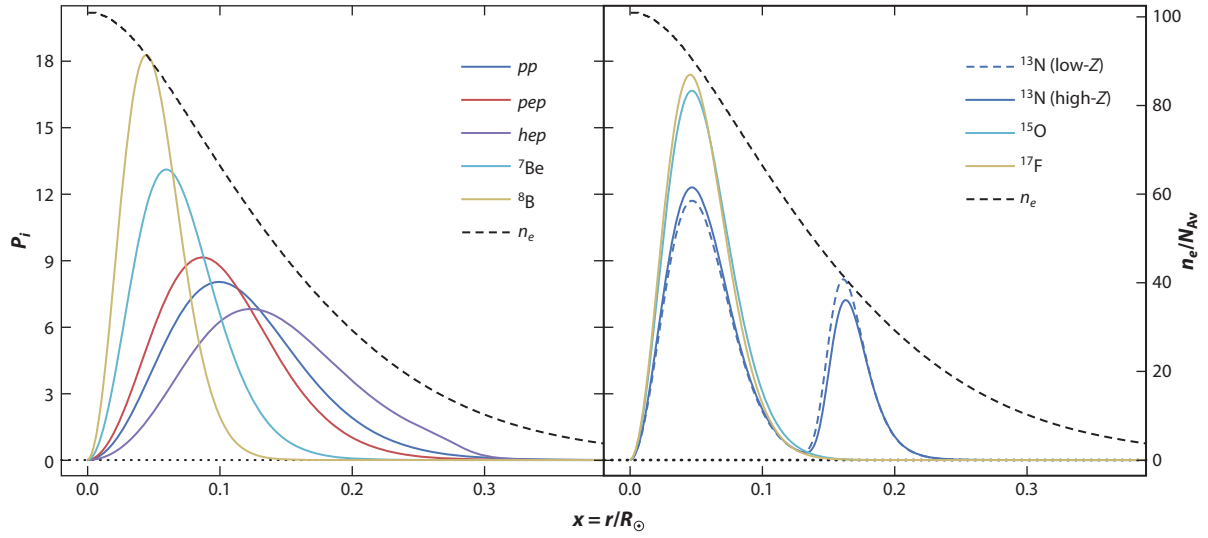

Figure 6

Probability distribution function of production for all solar neutrino fluxes ($\int_0^1 P_i dx = 1$, with i running over all fluxes). (*a*) Neutrinos from the *pp* chain. (*b*) Neutrinos from the CNO cycle. For $\Phi(^{13}N)$, distributions from a high-Z (*solid dark blue line*) and a low-Z SSM (*dashed dark blue line*) are shown. Both panels show the electron density (n_e) distribution in units of cm^{-3} mol^{-1}. Results based on SSM-B16 (4).

neutrino fluxes by using all neutrino data posterior to 2016 is missing in the literature, with recent work instead focusing on determination of the neutrino oscillation parameters (156, 157).

SSM neutrino fluxes and uncertainties are given in **Table 1** for the B16 high-Z and B16 low-Z models. Metals affect solar neutrinos by modifying the core temperature in the Sun, and as a result, the stronger the temperature dependence of neutrino fluxes, the larger the difference between the high-Z and low-Z predictions. Such dependence is primarily responsible for the distribution of the production of neutrino fluxes in the solar interior, as illustrated by the production probability distribution functions in **Figure 6**. CNO fluxes carry an additional dependence on the C, N, and O abundance in the solar core. The distribution profiles are insensitive to the solar composition, with the exception of $\Phi(^{13}N)$. The external peak in its distribution is produced by the production of N from primordial C in the Sun. It is therefore proportional to the C abundance and is largely independent of environmental factors and uncertainty in the $^{12}C(p, \gamma)^{13}N$ reaction (71). The second, inner peak comes from the CN cycle operating in steady state, which depends not only on the total abundance of C+N but also on the temperature of the solar core—that is, it is affected by environmental factors. Its importance is therefore smaller in low-Z solar models, as seen in **Figure 6**. Overall, the difference in radial distributions between the two models is very small and should have a negligible contribution to the integrated survival probability of $\Phi(^{13}N)$ neutrinos. The electron density, on which Mikheyev–Smirnov–Wolfenstein (MSW) effects depend, is also shown in **Figure 6**.

The possibility of using solar neutrinos to discriminate between low-Z and high-Z solar models with currently available solar neutrino data, limited to fluxes from the *pp* chain, leads to inconclusive results (4), as given in the last row of **Table 1**. Moreover, such comparison is sensitive only to the temperature in the solar core—that is, to the radiative opacity—and not directly to the solar composition (158). Another possible test between low-Z and high-Z models that is also sensitive to core temperature is the comparison of the ratio $R_{I/II}$ (23), the relative intensity of the *pp*-I and *pp*-II

chains, which is determined experimentally as $R_{\mathrm{I/II}} = 2\Phi(^7\mathrm{Be})/[\Phi(pp) - \Phi(^7\mathrm{Be})]$. Borexino results yield $R_{\mathrm{I/II}} = 0.178^{+0.027}_{-0.023}$ and the global fit 0.176 ± 0.015. Results for the SSMs are 0.180 ± 0.012 and 0.161 ± 0.011 for the B16 high-Z and B16 low-Z models, respectively. Current experimental results seem to favor SSMs with higher core temperatures, as stated in Reference 23.

Using solar neutrinos to break the degeneracy between opacities (i.e., solar core temperature) and composition is possible only with neutrinos from the CNO cycle (63, 70, 158, 159). By separating the dependence on environmental factors, nuclear reactions, and CN abundances, a relation between $\Phi(^8\mathrm{B})$ and $\Phi(^{13}\mathrm{N})$ or $\Phi(^{15}\mathrm{O})$ (or a linear combination of the latter two) can be established, with the role of solar models limited to that of scaling factors (63, 70). Recently, References 71 and 160 determined this relation, taking into account the differential sensitivity of the Borexino detector to $^{13}\mathrm{N}$ and $^{15}\mathrm{O}$ neutrinos, and obtained

$$\frac{\Phi^{\mathrm{BX}}(\mathrm{CN})}{\Phi^{\mathrm{BX}}_{\mathrm{SSM}}(\mathrm{CN})} = \left[\frac{\Phi(^8\mathrm{B})}{\Phi_{\mathrm{SSM}}(^8\mathrm{B})}\right]^{\alpha} \left[\frac{X_{\mathrm{C}}}{X_{\mathrm{C,SSM}}}\right]^{0.814} \left[\frac{X_{\mathrm{N}}}{X_{\mathrm{N,SSM}}}\right]^{0.191} \left[\pm 9.1\%\ (\mathrm{nucl.}) \pm 0.5\%\ (\mathrm{env.})\right], \quad 8.$$

where $\Phi^{\mathrm{BX}}(\mathrm{CN}) = (1 - \xi)\Phi(^{13}\mathrm{N}) + \xi\Phi(^{15}\mathrm{O})$, with $\xi = 0.764$, is the combination of fluxes that the Borexino detector is sensitive to; X_{C} and X_{N} denote carbon and nitrogen mass fractions, respectively; and the SSM subindex denotes SSM values. The relation can be simplified further to an almost linear relation between $\Phi^{\mathrm{BX}}(\mathrm{CN})$ and $(X_{\mathrm{C}} + X_{\mathrm{N}})$ if the fractional change of C and N with respect to the values in the SSM is assumed to be the same (70). Note that dependencies on all environmental factors are almost perfectly canceled out by the relation with $\Phi(^8\mathrm{B})^{\alpha}$, which makes the above expression rather insensitive to uncertain quantities, such as radiative opacities, and also valid beyond the framework of SSMs. The value of the exponent, $\alpha = 0.716$, is specific to $\Phi^{\mathrm{BX}}(\mathrm{CN})$. Analogous relations can be easily obtained (70, 71) for future detectors simply by determining ξ and α according to the differential sensitivity of the detector to $\Phi(^{13}\mathrm{N})$ and $\Phi(^{15}\mathrm{O})$. If future experiments allow separate measurements of $\Phi(^{13}\mathrm{N})$ and $\Phi(^{15}\mathrm{O})$, the difference $\Phi(^{13}\mathrm{N}) - \Phi(^{15}\mathrm{O})$ can be used to determine the C abundance independently of N, which can then also be determined.

Motivation for measuring neutrino fluxes from the CNO cycle goes well beyond the solar abundance problem. After a very short initial phase of about 1 Myr according to SSMs, and an even shorter one in other solar formation scenarios (161), the solar core has been isolated from the rest of the solar system. Its composition is a fossil record of the primordial composition of the cloud from which not just the Sun, but all the planets, formed. Moreover, the comparison between the core and surface abundance of metals could be used to determine the efficiency of mixing processes in the Sun—processes for which there are no direct constraints so far, which are needed for precision solar and stellar modeling.

5. SOLAR NEUTRINO PHYSICS

5.1. Solar Neutrino Flavor Change

Observations of the Z^0 boson decay width show that there are only three neutrinos with masses less than half of the Z^0 width (i.e., 45 GeV). This is consistent with limits from big bang nucleosynthesis (162). Hence, flavor and mass eigenstates are linked with a unitary 3×3 matrix called the Pontecorvo–Maki–Nakagawa–Sakata (PMNS) matrix (163). Any 3×3 matrix can be parameterized by three mixing angles θ_{12}, θ_{13}, and θ_{23} and a complex phase $e^{i\delta}$. [A Majorana mass term for neutrinos would introduce two additional complex phases, but these are relevant only for neutrino-less double β decay (NLDBD) searches.] Hence, there are mass eigenstates (ν_1, ν_2) and (ν_3) and flavor eigenstates (ν_e, ν_μ, and ν_τ), which are linked by the PMNS matrix.

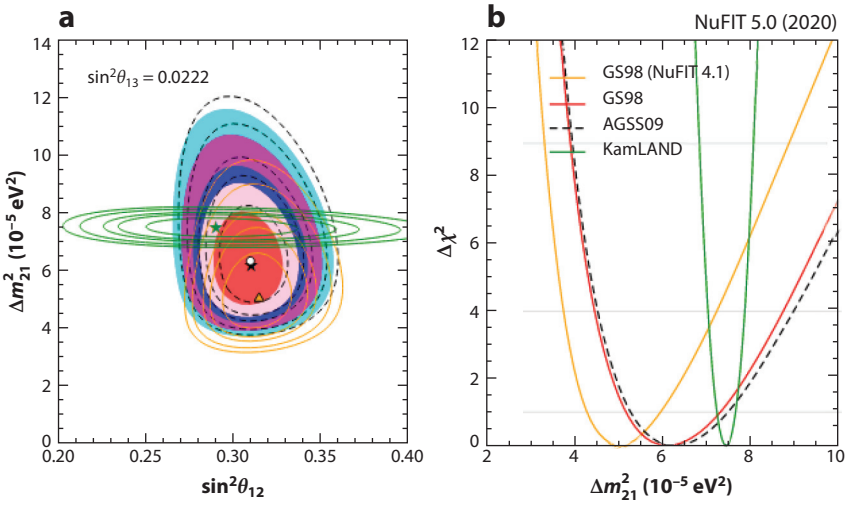

Figure 7

Current status of solar neutrino oscillation parameters. (*a*) Allowed parameter regions (1σ at 90%, 2σ at 99%, and 3σ CL for 2 degrees of freedom) from the combined analyses of solar data for the GS98 model (50) (*filled regions* with best fit marked by *black star*) and the AGSS09 model (45) (*dashed void contours* with best fit marked by a *white dot*) and for the analysis of KamLAND data (*solid green contours* with best fit marked by a *green star*) for fixed $\sin^2\theta_{13} = 0.0222$ ($\theta_{13} = 8.6°$). Also shown are the previous results of the global analysis for the GS98 model (50) (*solid orange contours*). (*b*) The $\Delta\chi^2$ dependence on Δm^2_{21} for the same four analyses after marginalizing over θ_{12} (157). Figure adapted from Reference 157 (CC BY 4.0).

This is analogous to the well-known Cabibbo–Kobayashi–Maskawa (CKM) matrix in the quark sector. The values of the matrix elements have to be determined experimentally. Results of mass eigenstates $m_{i,\,i=1,2,3}$ are presented in the form of $\Delta m^2_{ij} = m^2_j - m^2_i$. Besides solar data, reactor, astrophysical, atmospheric, and long-baseline neutrino beams also contribute to the determination of the PMNS matrix. The current status of its element values can be found in Reference 157 and is shown graphically in **Figure 7**. Based on all available solar neutrino data, a consistent picture appears for the survival probability as mentioned in Section 1.

Global solar neutrino data show that matter effects play a critical role. The weak scattering of electron neutrinos off electrons in the Sun has a larger cross section than that of muon and tau neutrinos because of the presence of CC as well as NC channels. This results in an additional effective mass term that modifies the effective mass difference between states and introduces off-diagonal terms into the neutrino mixing matrix, which further enhance vacuum oscillation. In effect, the neutrino eigenstates are modified in matter, with an effective mixing angle that can take the maximal value of unity under certain conditions. In 1986, Mikheyev & Smirnov (164) discovered these matter-enhanced neutrino oscillations by numerically propagating solar neutrinos through the Sun while taking into account the flavor-dependent index of refraction, a phenomenon first explored by Wolfenstein (165). Several key papers published that same year explored this phenomenon in terms of quantum mechanical level crossing and reproduced the numerical results with analytical methods (166–168). The conditions for this so-called MSW oscillation are realized in the solar core for higher-energy solar neutrinos, causing them to be created in the matter-modified ν_2 state. Adiabatic conversion as they propagate through the Sun results in neutrinos exiting in the vacuum ν_2 state, leading to a survival probability of $\sin^2\theta_{12}$.

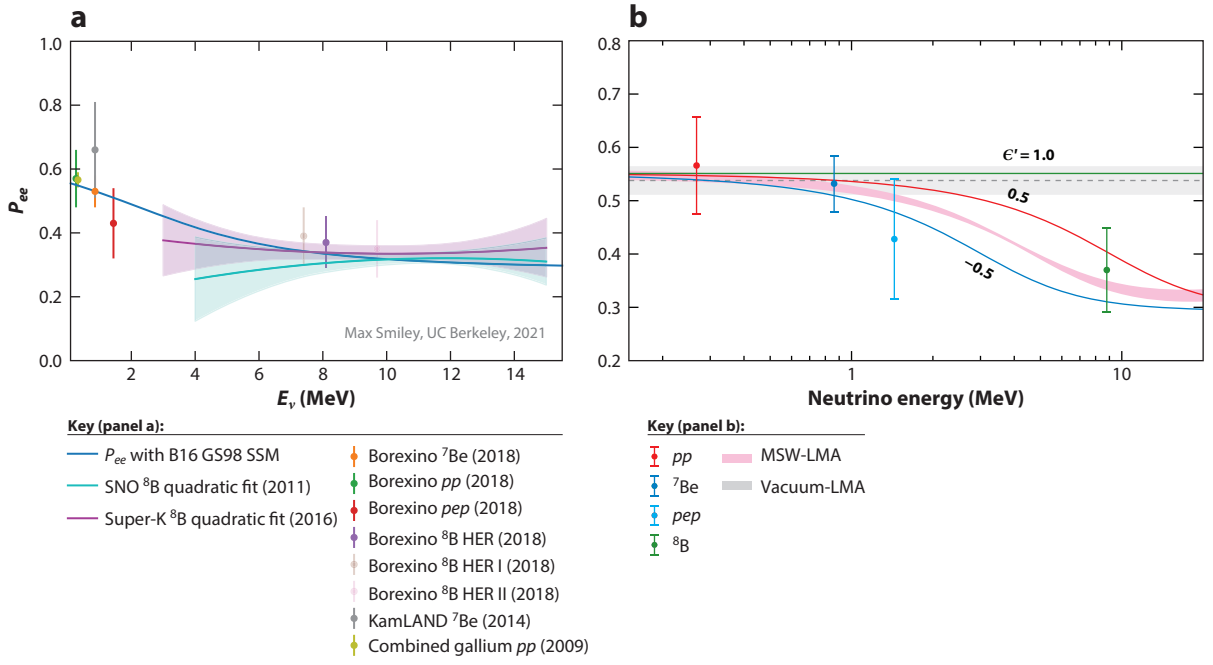

Figure 8

(*a*) The electron neutrino survival probability curve as a function of neutrino energy (linear). Experimental data (11, 15, 23, 237, 248) from various experiments are shown. Panel provided by M. Smiley, University of California, Berkeley. (*b*) Same kind of plot (now logarithmic) showing the survival probability as before but in this case for some representative curves for the nonstandard interaction parameter ϵ' for values of 1.0, 0.5, and −0.5. Also shown are the vacuum-LMA and MSW-LMA curves (from Reference 169). Panel adapted from Reference 169 (CC BY 4.0). Abbreviations: LMA, large mixing angle; MSW, Mikheyev–Smirnov–Wolfenstein; SSM, standard solar model.

The effect of MSW oscillation can be observed in the electron neutrino survival probability curve (**Figure 8**). At low energies (less than about 2 MeV), vacuum oscillations dominate, whereas matter effects dominate at energies above about 5 MeV. Between these two regimes is the so-called transition region with limited data. This region is in fact the most sensitive to potential nonstandard physics (Section 5.2) because of the level-crossing phenomenon that arises due to the different effective masses for electron neutrinos and muon or tau neutrinos in matter. The lowest measured high-energy data point suggests a certain upturn at the lower part of the curve, but this is not statistically significant. The uncertainties on most measurements are on the order of several percent. Hence, the constraints allow for various shapes of the survival probability curve and, thus, potentially also for interesting physics. These possibilities open a wide field for experimental exploration. Probing the transition region is one focus of the future experimental program, which is discussed in more detail in Section 6.

Day/night effect: an asymmetry in the electron neutrino flux measured during the day versus the night due to regeneration of electron neutrinos during passage through the Earth

At higher energies (above approximately 10 MeV), a distortion is predicted in the spectrum due to regeneration of electron neutrinos as they traverse the Earth during the nighttime. This is termed the day/night effect and has been sought by several experiments but, to date, remains elusive because of the small nature of the predicted effect (1–3%) (170). The significance of the predicted effect depends critically on the value of Δm^2_{12}: Smaller values result in a larger MSW effect in the Earth and, hence, a larger day/night asymmetry. This dependence offers one possible handle on a currently small discrepancy between the measured values of Δm^2_{12} in solar data and

in KamLAND's terrestrial reactor data (171). Seasonal variations in the solar neutrino flux have also been observed and are consistent with the eccentricity of the Earth's orbit, and there is no evidence for additional vacuum oscillation effects (172).

Almost all the solar fusion reactions except for the *hep* flux have been observed (Section 4). The *hep* flux has the highest energy but a low flux, and it extends beyond the ^{8}B spectrum in only a small window. It also interferes with attempts to observe the diffuse supernova neutrino background (DSNB), which is an interesting study in its own right. A one-sided limit of the *hep* flux of $\Phi_{hep} < 30 \times 10^3$ cm^{-2} s^{-1} is given by the SNO experiment (173).

NSI: nonstandard interaction

5.2. Nonstandard Interactions

As the uncertainties on many neutrino measurements are several percent or more, there remains potential for physics beyond the Standard Model. A first topic to explore regarding the survival curve involves the introduction of nonstandard interactions (NSIs) (174, 175). At low neutrino energies, a four-fermion interaction vertex can be described by

$$\mathcal{L}^{\mathrm{NSI}} = -2\sqrt{2}G_F(\bar{\nu}_\alpha\gamma_\rho\nu_\beta)(\epsilon^{f\tilde{f}_L}_{\alpha\beta}\bar{f}_L\gamma^\rho\tilde{f}_L + \epsilon^{f\tilde{f}_R}_{\alpha\beta}\bar{f}_R\gamma^\rho\tilde{f}_R) + \mathrm{h.c.} \quad 9.$$

Here the ϵ terms denote the strength of the NSI between the neutrinos ν of flavors α and β and the left- and right-handed components of the fermion f. In this way, experimental data are needed to constrain all these parameters, some of which have already been excluded by former experiments (176).

Results from the Borexino experiment constrain the values of these parameters (169). Future sensitivity studies have been performed for a combination of three experiments—Hyper-Kamiokande (Hyper-K), DUNE, and MICA (177)—as well as for the DUNE near detector (178). As the ϵ' parameters at first order are mostly degenerate, studies have been performed to disentangle these parameters (179).

Searches for solar antineutrinos have been performed by the SNO (180), Super-K (181), and, more recently, Borexino experiments (182). A potential source is the flux from the ^{40}K decay within the Sun, which produces an antineutrino flux of about 200 $\bar{\nu}_e$ cm^{-2} s^{-1} on Earth. However, the terrestrial ^{40}K background is overwhelming. Above 3.2 MeV, the upper threshold for ^{40}K-decay photofission processes in the Sun can provide higher-energy antineutrinos (183). Nonstandard physics processes also produce electron antineutrinos, and, in turn, they can be constrained by measurements (184). Another source that has been debated for a long time is highly energetic solar flares, which might produce pions in the solar atmosphere and thus produce neutrinos (185).

Several other nonstandard physics effects can affect the shape of the ν_e survival probability in the transition region. Mixing of the three known neutrino states with a light sterile neutrino could modify the shape of the spectrum in the transition region through an additional suppression of the ν_e survival probability caused by the addition of a new mass state, m_4 (186, 187). Improved precision in measurements of the ^{8}B spectral shape and the *pep* flux would be most sensitive to this effect. Sterile neutrinos, like right-handed singlets in the Standard Model, would allow for significant extensions of the neutrino sector. For symmetry reasons, three singlet states could be imagined. This would considerably extend the mixing matrix. A neutrino magnetic moment would modify the ES cross section with an enhancement at low energies. The ^{7}Be line source and the spectrum of low-energy neutrinos are useful probes of this effect. A magnetic moment can be created by a one-loop diagram resulting in the following (188):

$$\mu_\nu = \frac{3eG_F}{8\sqrt{2}\pi^2}m_\nu = 3.2 \times 10^{-19}\left(\frac{m_\nu}{\mathrm{eV}}\right)\mu_B. \quad 10.$$

Experimental searches are based on electron antineutrino–electron scattering searches at reactors and from astrophysical processes, especially the energy loss of red giant branch (RGB) stars (see Section 5.3). The current best limits from solar neutrinos come from the Borexino Collaboration's studies of ^{7}Be (148) and the low-energy solar neutrino spectrum (189).

The SNO experiment has produced limits on the lifetime of the second neutrino state (ν_2) from a study of the ^{8}B spectral shape (190). Limits on neutrino lifetimes also exist from cosmological studies (191).

5.3. Emission of (Un)known Particles

Another area of solar physics is the search for solar axions or more general ALPs (192, 193). The axion is a pseudoscalar object like the π^0. It can decay into two photons via a triangle graph with a coupling constant $g_{a\gamma}$. In a crossed Feynman diagram where one photon is provided from an external electromagnetic field, a monoenergetic γ-ray line will be generated (the Primakoff effect). The axion can be searched for in stellar objects like the Sun via the Primakoff effect $\gamma + Ze^- \rightarrow a + Ze^-$. Axions may play an important role in cosmology. Based on the Primakoff process, constraints on $g_{a\gamma}$ from astronomical objects have been deduced, and now experimental observations are split into two groups: haloscopes to search for cold dark matter in the Milky Way and helioscopes to search for a thermal solar axion flux.

A first limit on axion parameters can be deduced from astrophysics using the age of the Earth. Currently, the Sun is about halfway through its main sequence evolution. Hence, the solar axion luminosity must not exceed its photon luminosity; if it did, its nuclear fuel would be spent before reaching the current age of the Sun. This requirement puts constraints on the coupling $g_{a\gamma} \leq 2.4 \times 10^{-9}$ GeV^{-1}. The solar axion spectrum has been calculated in References 194 and 195. This provides an energy region of interest for experimental searches between 1 and 9 keV—that is, the X-ray region.

As with solar neutrinos, experiments searching for axions are often performed underground. A number of such searches have been performed (192), and further experiments are in preparation or under consideration to explore the parameter space (196). Independent constraints come from astrophysics—for example, from helioseismology (151, 197). Most of these studies are based on energy loss arguments (195, 198), in which axions add another component of energy loss in stars. The energy loss mechanism is especially important at the RGB (199). Additional stellar energy losses will affect the Hertzsprung–Russell diagram, which governs the evolution of stars. Energy loss arguments can be applied to studies of globular clusters with a decent number of stars to deduce limits on the axion (194) and can also produce limits for a magnetic moment of the neutrino (199).

6. DETECTION OF SOLAR NEUTRINOS

The main challenges for the next generation of solar neutrino measurements lie in a trifecta of requirements: scale, cleanliness, and depth. The sheer size needed for solar neutrino detection has been a requirement of long standing because of the weak nature of neutrino interactions. The exquisite precision now demanded for further discovery places even more stringent requirements on both depth (to restrict cosmogenic muon-induced backgrounds) and cleanliness. It is worth noting the importance of the shape of a site's overburden in evaluating the total muon rate: A flat overburden offers significant advantage in reducing the total rate of muons.

Detection of neutrinos is extremely challenging because of their very low reaction cross sections. ES of neutrinos on electrons is sensitive to all three flavors but with a significant (factor of approximately 6.5) enhancement for electron neutrinos. A great advantage of the ES reaction is the strong correlation between the direction of the outgoing electron and that of the incoming

neutrino, giving a pointing capability. The cross section for electron neutrinos undergoing ES is on the scale of 10^{-45} to 10^{-43} cm^2 across the full range of solar neutrino energies, hitting 4.3×10^{-44} cm^2 at 5 MeV, with a rising energy dependence. The CC reaction occurs only for electron neutrinos at energies relevant for solar neutrinos. This reaction has a more peaked differential cross section than the very broad ES dependence, offering a more precise measurement of incident neutrino energy. The reaction also has a weak angular correlation. The cross section for interaction on a deuteron is approximately an order of magnitude higher than that for ES at 5 MeV, at 3.5×10^{-43} cm^2 (200), although the number of available targets in a detector such as SNO is significantly lower than for ES. The CC reaction on ^{7}Li is almost an order of magnitude higher than that on the deuteron at 5 MeV, at 1.5×10^{-42} cm^2 (201), although both fall off rapidly at lower energies. A target-weighted cross section for a water, heavy water, and 10% Li-loaded detector is presented in Reference 202. CC reactions on ^{71}Ga (203) and ^{37}Cl (204) have been used to great effect in radiochemical experiments, although the respective cross sections are approximately 2 and 20 times lower than for ^{7}Li, in the range 2–5 MeV. Reference 205 presents a comparison of the CC reactions on Li, Cl, and Ga. An NC measurement offers flavor-blind neutrino detection. The cross section on the deuteron is 9.5×10^{-44} cm^2 at 5 MeV (200), more than a factor of two higher than the ES.

Next-generation experiments will focus on the ability to make a precise determination of the CNO neutrino fluxes for neutrinos produced in both the CN and NO cycles (Section 3.1), which would resolve questions in solar metallicity (Section 2). Improved accuracy in the measurement of the shape of the ^{8}B solar neutrino spectrum—particularly in the sensitive 1–5 MeV transition region between the low-energy, vacuum-dominated regime and the higher-energy, matter-dominated regime—would allow for tests of a number of nonstandard models, including flavor-changing NC interactions, and certain models for sterile neutrinos (Section 5). Precision measurements of the *pp* and *pep* fluxes can probe and monitor the solar luminosity (Section 4), ^{7}Be and ^{8}B can constrain the temperature of the solar core, and a measurement of the day/night asymmetry can constrain oscillation parameters and confirm our understanding of the interaction of neutrinos with matter.

6.1. Detection Techniques

Because of their weak interactions, large detectors are needed to gather enough statistics for precision measurements of solar neutrinos. Section 1 describes the tremendously successful program of experiments that first observed solar neutrinos, demonstrated neutrino flavor change and nonzero mass, and, more recently, moved into precision spectroscopy. These experiments fall into two main categories: radiochemical experiments and large, monolithic optical detectors. The former integrate over a period of many days or weeks to collect data and focus on integral flux measurements. For real-time detection and precision spectroscopy, large optical detectors have proved to be the workhorses of the field.

6.1.1. Radiochemical detectors. As discussed in Section 1, radiochemical experiments were critical in the understanding of the solar neutrino problem. The SAGE experiment is still operating, although it is largely focused on the so-called gallium anomaly related to a deficit in electron neutrinos observed from electron capture sources (12, 206). Radiochemical detection is still an area of active and ongoing research.

Perhaps the isotope with the lowest threshold for solar neutrino detection is ^{205}Tl, with a *Q*-value of only 52 keV, which triggered the idea for the LOREX experiment several decades ago (207). The daughter ^{205}Pb is very long-lived (half-life of several million years) and, thus, would not form a coincidence, but it would be an almost unique opportunity to measure the average solar neutrino flux over the last million years. The LOREX experiment is actively working on this

radiochemical approach. Recent nuclear cross section calculations on this reaction are predicting lower solar neutrino interaction rates than in the past (208). The bound state β decay, which was recently observed for the first time at the GSI research center in Germany, is an essential ingredient for such a potential ^{205}Tl measurement. Another nuclide that could provide information regarding the average neutrino flux over the last million years is ^{98}Mo (209).

6.1.2. Real-time detectors. The large, monolithic optical detectors used for real-time observations use either a water target or a scintillating liquid. In both cases, the target produces light in response to the passage of charged particles. Pure LS detectors offer high light yields, resulting in the extremely good energy resolution and low thresholds critical for addressing the vacuum-dominated regime of solar neutrino oscillation. They can also achieve impressively low levels of radioactive contamination; in this respect, the Borexino experiment has repeatedly paved the way with new standards in cleanliness. These ultraclean, high-light-yield detectors can target the lowest-energy solar neutrino fluxes and spectra, including the CNO, *pep*, and even *pp* neutrino fluxes. Water Cherenkov detectors offer the benefit of directional resolution for background rejection. The sheer volume of detector that can be constructed, thanks to the excellent attenuation lengths achievable with ultrapure water, can provide unprecedented statistics offering insights into both the ^{8}B spectral shape and day/night asymmetry. These two detector types are highly complementary, addressing opposite ends of the spectrum of solar neutrino physics.

In more recent years, a number of new developments could facilitate a new kind of experiment that might answer many of the critical open questions discussed in Sections 2 and 5. Perhaps the most promising avenue for next-generation detectors is the concept of a hybrid optical neutrino detector that could leverage both Cherenkov and scintillation signals in a single detector. This extremely challenging but potentially groundbreaking development could enable a new generation of detectors with world-leading sensitivity across a broad range of physics goals. For solar neutrinos, such an advance would enable directional detection to low thresholds as well as additional particle identification capabilities from the Cherenkov/scintillation ratio and the time profile of detected light. This enhanced capability could significantly improve background rejection and signal efficiency.

This hybrid detection can be achieved in a number of ways:

- by deploying a target material that modifies the scintillation signal in a number of ways, either by reducing the intensity (210–213) or by delaying the time profile (214, 215), to enhance separation from the fast, lower-intensity Cherenkov signal;
- by deploying fast photon detectors (216) to help differentiate prompt Cherenkov signals from the typically slower scintillation light; or
- by using spectral sorting to separate the Cherenkov and scintillation signals by their wavelength (217).

Substantial work has been dedicated to realizing this concept, both experimentally (218–222) and in the development of new analysis tools to leverage and enhance this simultaneous detection for large detectors (223–229).

The optimal configuration will depend on the exact detector geometry. For example, the long-wavelength tail of Cherenkov light travels more quickly than the predominantly blue scintillation. Thus, in a large detector, dispersion effects can enhance time-based signal separation; in a smaller detector, in which dispersion effects play less of a role, deployment of fast photon detectors may be more critical. The optimal configuration for any particular detector would involve optimization along all the above axes. It also would likely be determined, at least in part, by local factors, such as the practicalities of underground deployment of scintillators, readout requirements for different

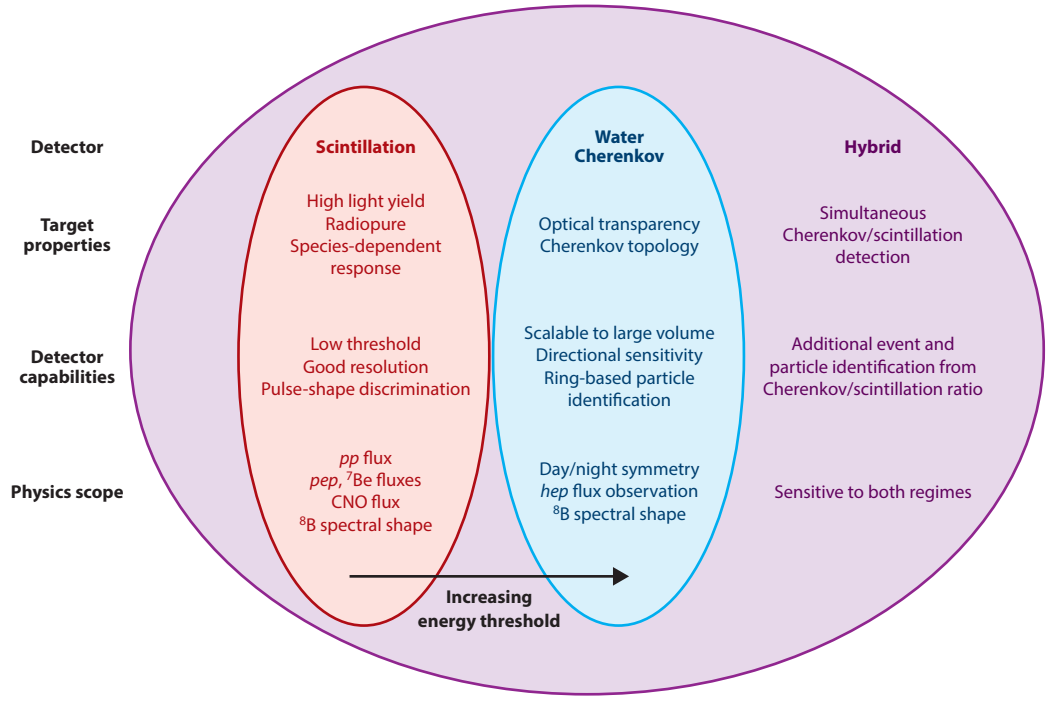

Figure 9

Conceptual illustration of the benefits offered by different real-time solar neutrino detection techniques and the physics they can address.

photon detector choices, and requirements related to other physics goals, which may place a premium on high light yields or, conversely, on a high-fidelity Cherenkov signal. **Figure 9** shows the benefits offered by each of these detector types and the solar neutrino physics they can address.

6.1.3. Isotopic loading. Isotopic loading can offer enhancements for solar neutrino detection—for example, by offering a CC detection channel, such as that used in the SNO experiment, which provides greater precision on the underlying neutrino spectrum. This may be important for probing details of the shape of the ^{8}B spectrum in the transition region between matter- and vacuum-dominated oscillation, for example. Various techniques are being explored to load large target masses while retaining the good optical properties critical for precision low-energy physics (230, 231). Candidates include ^{7}Li, which has a favorable cross section in the energy range relevant for probing the transition region.

The ^{100}Mo isotope is a candidate target for real-time measurements of *pp* neutrinos, with a low threshold and favorable cross section, and the signal has a nice coincidence with less than 1 min. A similar time coincidence can be formed from the double β decay (DBD) isotope ^{116}Cd (232). It is used in various NLDBD experiments, but solar *pp* detection is not possible as the *Q*-value is about 460 keV, just above the *pp* neutrino flux, making these two spectra difficult to disentangle. DBD isotopes with *Q*-values of more than 1 MeV exist, and they provide a potential target for solar *pp* neutrinos, especially ^{150}Nd (233).

A further potential nucleus for a *pp* measurement is ^{115}In. This nuclide was investigated in the LENS project (234), but activity waned in light of the challenge of achieving the required low background.

6.2. Water Cherenkov Experiments

Water Cherenkov detectors have played a critical role in some of the first solar neutrino results, including the original resolution of the solar neutrino problem. The ability to reconstruct particle direction allows solar neutrinos to "point back" to the Sun as their source, and allows discrimination from many sources of background.

6.2.1. Sudbury Neutrino Observatory and Super-Kamiokande. The first indication of a solution to the solar neutrino problem came from a combination of the CC measurement from SNO (20), which was sensitive only to the ν_e flux, with the high-statistics ES measurement from Super-K (235), which was sensitive to all three flavors, with an enhancement for the electron flavor. These two measurements disagreed at the 3σ level, demonstrating the presence of some non-electron-flavor neutrinos in the flux from the Sun. The SNO experiment's seminal NC measurement, which was equally sensitive to all three flavors, confirmed that the solar neutrino problem was due to the electron neutrinos produced in the solar core changing flavor before being detected on the Earth (21).

Both experiments have since improved the precision of ^{8}B flux and oscillation parameter measurements and have pushed toward low energy thresholds to probe the shape of the ^{8}B spectrum in the MSW transition region (15, 236, 237). To date, the measured spectral shape is consistent with the MSW-predicted upturn and also with several nonstandard effects (Section 5). Both experiments have sought evidence of the day/night effect (238, 239). Although Super-K initially saw a nearly 3σ indication of this effect, subsequent data were seen to reduce the significance. Greater statistics are required to confirm this effect. Future reactor data at Super-K may allow sufficient precision on Δm^2_{12} to resolve the current small discrepancies between reactor and solar data (171). A search for *hep* neutrinos is extremely challenging because of the very low predicted flux. The best limits on this flux come from SNO and are currently a few times the SSM prediction (173).

SNO ceased operation in 2006. More recent analyses of the data set have provided constraints on nonstandard effects such as Lorentz violation and neutrino decay (240, 241). The Super-K experiment continues to take data and will further improve on both statistics and precision for the ^{8}B measurements. Super-K has recently been upgraded with the addition of gadolinium in a project known as SK-Gd, which will enhance neutron capture efficiency (242, 243).

6.2.2. Hyper-Kamiokande. The Hyper-K experiment is expected to start construction and operation this decade (170). At a total mass >250 kt, with 40% coverage, Hyper-K has the potential to contribute much detail to the picture of high-energy solar neutrinos in particular.

The small day/night effect and the relatively flat spectrum measured by the SNO and Super-K experiments define the values of the oscillation parameters and result in some small tension with terrestrial measurements at the KamLAND experiment. Within 10 years of operation, the Hyper-K detector will be able to measure the day/night asymmetry to better than 4σ and 8σ at the values currently predicted, respectively, by reactor and solar experiments. The Hyper-K Collaboration also expects improved sensitivity to both the ^{8}B shape and *hep* neutrinos due to sheer size as well as improved light collection efficiency relative to Super-K.

6.3. Liquid Scintillator Experiments

Scintillator-based experiments offer significantly increased photon yield, which results in better energy resolution, and the ability to probe lower in neutrino energy. This offers a window into a new regime of physics.

6.3.1. Borexino. The high light yield of organic scintillators offers high-precision spectroscopy as well as low thresholds. The Borexino Collaboration has laid new ground for scintillator-based

detection of solar neutrinos, with world-first direct measurements of *pp* (155) and *pep* neutrinos (244), the best precision of ^{7}Be (148, 245), as well as ^{8}B flux and spectrum measurements. This comprehensive spectroscopic study of the *pp* chain of solar neutrinos (23, 24, 246) is complemented by the first detection of neutrinos from the subdominant CNO cycle (25), a groundbreaking achievement. This experiment will cease taking data shortly, but it has paved the way for a new generation of scintillator experiments to follow. One of the Borexino experiment's particular accomplishments was the astonishing level of radioactivity purity achieved in the detector: levels approaching 10^{-19} g/g of both ^{232}Th and ^{238}U and, most critically for the CNO measurement, a rate of ^{210}Bi events $\leq 11.5 \pm 1.3$ counts per day per 100 t of detector material (cpd/100t). This can be compared with the fitted CNO rate of $7.2^{+3}_{-1.7}$ cpd/100t. The main limiting factors to improved precision remain lingering sources of radioactivity, in particular these low levels of ^{210}Bi, and cosmogenic-induced backgrounds such as ^{11}C. A leading consideration for improved precision in the *pp* measurement is the ^{14}C background, which is inherent in any organic scintillator.

6.3.2. KamLAND. The KamLAND detector has a long history of discovery, including the seminal paper that demonstrated that the neutrino flavor change observed in the SNO experiment was in fact due to oscillation (26). Reactor measurements of the $\theta_{12}/\Delta m^2_{12}$ sector of oscillations with KamLAND data provide a terrestrial comparison to solar neutrino results, with some small tension persisting in the value of Δm^2_{21}. The KamLAND Collaboration has also made several measurements of solar neutrinos, including a measurement of the spectral shape of ^{8}B neutrinos at low energy (247) and detection of ^{7}Be neutrinos (248). Since then, the KamLAND detector has been upgraded for a world-leading NLDBD search (249, 250) with an inner containment vessel deployed in the center of the detector containing an Xe-loaded scintillator. This detector continues to be sensitive to solar neutrinos. Future measurement potential includes ^{8}B flux and spectral measurements as well as more exotic analyses, such as searches for solar antineutrinos.

6.3.3. SNO+. SNOLAB in Ontario, Canada, offers one of the deepest sites available worldwide for low-background studies, at a depth equivalent to 6 km of water. This feature results in incredibly low cosmogenic backgrounds, in particular the ^{11}C that can be a limiting factor in precision low-energy solar neutrino measurements. The SNO detector has been converted from a water Cherenkov detector to a pure LS detector as part of the program for the SNO+ experiment (251). The primary goal for SNO+ is a search for NLDBD via loading of the LS with tellurium. Like KamLAND-Zen, this detector will have sensitivity to solar neutrinos, in particular the ^{8}B neutrinos that lie above the $2\nu\beta\beta$-decay end point of ^{130}Te (approximately 2.5 MeV) (252). SNO+ will be the deepest low-background neutrino experiment operating, and, given its scintillating target mass of 780 t, a future phase of the experiment has the potential to contribute across the breadth of solar neutrino physics.

Early data from the initial water phase of SNO+ have already demonstrated low levels of cosmogenic and external background, allowing a measurement of the ^{8}B spectrum in water (253). LS data should allow improved precision and a significantly lower threshold. Preliminary LS data from SNO+ show levels of radon daughters in the detector that would make low-energy solar neutrino measurements challenging. Precision measurements of this regime would require significant reduction of these backgrounds, similar to that achieved during the first period of Borexino operations (148). This issue could potentially be addressed via an extensive campaign that would include recirculation through the SNO+ scintillator process systems, built with several purification capabilities, along with other background reduction techniques.

Estimates of the SNO+ sensitivity to CNO neutrinos can be made under the assumption of certain levels of background reduction. The radiopurity levels observed in early LS data already

meet the targets for the primary goal of NLDBD and might be sufficient to permit a limited-precision measurement of the CNO flux with large uncertainties due to the presence of backgrounds. With significant further background reduction by approximately a factor of 10 for the U and Th chains and 1,000 for ^{210}Bi, negligible ^{40}K, and constraints on the *pep* flux based on the *pp* flux [as was done by the Borexino Collaboration in their discovery paper (25)], SNO+ could achieve better than 15% precision on the CNO flux.

SNO+ will also offer improved precision in Δm^2_{12}. Sensitivity to this parameter using both solar neutrinos and reactor neutrinos will provide additional data to resolve current (small) discrepancies in measurements from solar and terrestrial sources.

6.3.4. JUNO. The Jiangmen Underground Neutrino Observatory (JUNO) is due to start construction in 2021 with data taking to follow within a few years (254, 255). At 20 kt, with approximately 75% coverage, a goal of 3% energy resolution at 1 MeV, and a target of 10^{-17} g/g intrinsic ^{238}U and ^{232}Th, the JUNO experiment will be a groundbreaking achievement in low-energy neutrino detection. JUNO's primary goal is to measure the neutrino mass hierarchy using reactor neutrinos. The relatively shallow overburden of 680 m limits the low-energy solar neutrino program. However, at the target background levels, a threshold of 2 MeV could be achieved for ^{8}B neutrinos. This threshold is substantially lower than that achievable in a Cherenkov detector and is even 1 MeV lower than that achieved by the Borexino detector for a measurement of the ^{8}B spectral shape (256). Combined with the large volume, which results in rapid collection of statistics, the JUNO detector will have sensitivity to NSIs that could affect the ^{8}B spectral shape as well as 2σ and 3σ sensitivity to the day/night effect at current reactor- and solar-favored parameter values, respectively (257). With the ability to measure Δm^2_{12} to percent-level precision from reactor neutrinos and to approximately 20% using solar neutrinos, the JUNO detector will provide a uniquely precise cross-check on the consistency of data from these two sources. Precision measurements of the ^{7}Be and ^{8}B fluxes are also possible.

6.4. Hybrid Optical Neutrino Detectors

Hybrid optical neutrino detectors would leverage both the unique topology of Cherenkov light and the benefits of high-yield scintillation in the same detector. This offers the potential for significant improvements in event imaging capabilities, and discrimination of signal from background.

6.4.1. Jinping. The Jinping underground laboratory in China (258) has a 2.4-km rock overburden, which results in a cosmic-ray muon flux almost as low as that at SNOLAB (259). A 5-kt scintillator detector is planned at this site; the goal is to deploy a high-light-yield organic scintillator with careful target selection and high-precision, high-coverage instrumentation such that the Cherenkov signal can be leveraged for direction reconstruction and particle identification. Data from a 100-t-scale prototype could be available as early as 2024. The depth, size, and hybrid optical detection could allow for unprecedented precision in solar neutrino measurements. The Jinping Neutrino Experiment would have sensitivity across the full spectrum of solar neutrinos. The letter of intent for the experiment explores the capabilities for a range of detector sizes and light collection values: 1 to 4 kt in fiducial mass and a light collection range of 200 to 1,000 photoelectrons per MeV (260). The highest-performing detector under consideration would achieve percent-level measurements of the *pp*, ^{7}Be, and ^{8}B neutrinos as well as a few-percent uncertainty on the *pep* neutrino flux. A CNO measurement is highly dependent on both target mass and resolution, but it could reach better than 15% precision for the larger, high-resolution detector configurations. The experiment would also have good sensitivity to probe the ^{8}B spectral shape.

6.4.2. THEIA. THEIA, a proposed large-scale hybrid optical neutrino detector (202), is a realization of the advanced scintillation detector concept first proposed in Reference 205. With plans to include both water-based LS (WbLS) and other novel LS materials and isotopic loading options, along with cutting-edge photon detection technology, THEIA's proposed site at the Sanford Underground Research Facility (SURF) laboratory in South Dakota (United States) would offer a high-energy neutrino program as part of the Long-Baseline Neutrino Facility, as well as a broad program of low-energy physics. Although pure LS offers improved radiopurity, directional sensitivity would at least in part offset the increased levels of contamination inherent in the water component of a WbLS target. At its full, 50- to 100-kt size, THEIA could achieve better than 10% precision on CNO solar neutrinos with a WbLS target, or percent-level precision with pure LS (202, 261, 262). This precision would allow a high-confidence resolution of the metallicity problem. Possible isotope loading is also being explored to offer a CC interaction, which would provide a high-fidelity measure of the underlying neutrino spectrum, potentially offering enhanced sensitivity both to CNO neutrinos and to the ^{8}B spectral shape.

Fluor: material added to scintillator that shifts the spectrum of emitted light to a region chosen to enhance photon propagation

PPO: 2,5-diphenyloxazole

Even a small, few-hundred-tonne hybrid detector could offer enticing reach for solar neutrinos if filled with a high-light-yield material, as explored in Reference 262. That study assumed a standard scintillator mixture of linear alkylbenzene (LAB) loaded with 2 g L^{-1} of the fluor, 2,5-diphenyloxazole (PPO),[3] and assessed the impact of different photon detectors. With current standard photomultiplier tubes (1.6-ns transit time spread), such a detector could achieve 14% precision on the CNO neutrino flux, dropping below 10% if a constraint is imposed on the *pep* flux based on knowledge of the *pp* flux, as done by the Borexino Collaboration in their discovery paper (25). With fast photon detectors, such as LAPPDs (large-area picosecond photodetectors) (216), the precision is below 5%. Slow fluors, such as those studied in References 214 and 215, can further enhance the separation of the prompt Cherenkov signal by delaying the scintillation light and may offer further performance improvements, although this effect must be balanced against potential degradation in vertex reconstruction due to reduced precision in photon time-of-flight information.

6.4.3. Other hybrid detectors. A group in Korea is exploring the option for a few-kilotonne-scale detector in the Yemilab (263). Both a WbLS and a pure scintillator are under consideration.

6.5. Noble Liquid and Solid-State Experiments

As experiments continue to break new ground, solar neutrinos can become a background for other searches and thereby offer new opportunities for discovery. Experiments designed to search for coherent neutrino-nucleus ES, known as CEνNS, will be sensitive to higher-energy solar neutrinos via this channel. Although CEνNS interactions were proposed many decades ago (264–266), they were only recently detected experimentally, at Oak Ridge (267, 268). The cross section for CEνNS interactions is favorable because of an A^2 dependence; however, since the nuclear scatters typically fall below 10 keV, detectors with excellent resolution and very low threshold are required. Next-generation noble liquid dark matter experiments designed to search for nuclear recoils from weakly interacting massive particle interactions will be sensitive to the so-called neutrino floor, where solar neutrinos, among other sources, have the potential to become a dominant background (269). Sensitivity in these detectors comes via two channels: CEνNS above 5 MeV and ES in the keV–MeV range.

[3] Fluors can affect both the number and time profile of emitted photons. Adding 2 g L^{-1} of PPO enhances the light yield of LAB by approximately an order of magnitude and shortens the time profile significantly, resulting in improved vertex reconstruction.

6.5.1. Solid-state detectors. A combined CEνNS and ES signal in a tonne-scale Ge detector would offer improved sensitivity to the shape of the survival probability curve across the range from vacuum- to matter-dominated oscillation and would also provide sensitivity to possible active-to-sterile mixing (270).

Extremely low-threshold detectors, such as SuperCDMS, might potentially detect *pp* and other low-energy branches via this route if thresholds in the few-eV range can be achieved (271, 272). Equaling the precision of the Borexino measurements would require exposure on the scale of 500 kg·year for *pp* and ^{7}Be neutrino fluxes and 5,000 kg·year for *pep* and CNO fluxes (273).

6.5.2. Noble liquid detectors. An advantage of these inorganic scintillating materials is the lack of intrinsic ^{14}C background, which forms a dominant background to *pp* flux measurements in organic scintillators. Noble liquid detectors also offer excellent discrimination between electron- and nuclear-recoil signatures.

A large liquid xenon (LXe) detector would have sensitivity to ^{8}B neutrinos in the 5–15 MeV range via CEνNS, which could offer a sensitive test of the spectral shape in this region, probing the possible presence of NSIs and allowing discrimination between the presence of NSIs and a possible dark-side solution for oscillation parameters ($\theta_{12} > 45°$) (274–279). A search for such events in the XENON1T experiment did not observe a signal but does show promise for a discovery in the forthcoming XENONnT experiment (280). Improved resolution in the few-keV nuclear recoil energy range could permit discrimination and first discovery of the *hep* neutrinos.

Electron recoils from ES interactions give rise to signatures of tens to hundreds of keV. High light yield and excellent energy resolution would allow studies of *pp* and other low-energy, high-flux branches with good precision via this channel. A percent-level ES measurement of *pp* neutrinos may be possible in a large LXe detector such as DARWIN (281–283), which aims for 50 t of LXe. This would require either depletion of ^{136}Xe or a focus on the very low-energy regime, where the $2\nu\beta\beta$ spectrum falls rapidly. This approach may also offer a path to the lowest-energy measurement of $\sin^2\theta_W$ if one independently imposes the LC. This scenario assumes significant reductions in radiopurity beyond current-generation detectors—that is, a reduction by nearly three orders of magnitude to approximately 10 events per tonne-year per keV in the electron recoil band. Another background would come from neutrino capture on ^{131}Xe (21% abundance), which would add events in the region of 355 to 420 keV, relevant for a *pp* measurement. New nuclear cross section calculations show increased solar neutrino interaction rates (284). If the $2\nu\beta\beta$ spectrum could be reduced by three orders of magnitude, a measurement of CNO neutrinos might be possible (285).

The projected 1,000-tonne-year exposure of a next-generation two-phase liquid argon (LAr) TPC would collect over 10,000 CNO ES events and offer sensitivity to ^{7}Be and *pep* neutrinos. Flux measurements would require radon reduction of about three orders of magnitude beyond that measured in smaller detectors, to 200 μBq of ^{222}Rn per 100 t (equivalent to 16 cpd/100t), although this issue is expected to be at least partially mitigated by the additional shielding of a larger detector. This background rate can be compared with a predicted CNO rate above threshold of 0.64 cpd/100t for low-Z models and 0.90 cpd/100t for high-Z models. Underground argon (UG-Ar) is also required in order to limit the impact of other backgrounds. The DarkSide-50 experiment demonstrated levels of ^{39}Ar in UG-Ar over 10^3 lower than atmospheric argon at 0.7 mBq kg^{-1} (286). The β decay of ^{42}K, a daughter of ^{42}Ar, has an end-point energy of 3.52 MeV and contributes a potentially significant background in the region of interest. Measurements of atmospheric argon show ^{42}Ar activity of 94.5 ± 18.1 μBq kg^{-1} (287), which is equivalent to $\sim 8 \times 10^5$ cpd/100t. Studies assume this background would be significantly reduced by the use of UG-Ar, such that it can be neglected. With these assumptions, such a detector could achieve

precision on CNO of approximately 17% for high-Z models and approximately 23% for low-Z models, and precision of a few percent for ^{7}Be (288).

Detection via CC interactions has been studied for both LXe and LAr detectors. CC capture on ^{136}Xe offers a delayed coincidence signal, which could provide a low-background approach for CNO neutrino detection, and a precision measurement of the ^{7}Be energy, yielding insight regarding the core temperature of the Sun (289).

The long-baseline neutrino experiment, DUNE, will have sensitivity to high-energy solar neutrinos via both ES and CC interactions in the LAr target (290). Above 5.9 MeV, CC interactions on ^{40}Ar result in transitions to excited states in ^{40}K (291) and offer good resolution for reconstructing the neutrino energy. While the threshold in this detector is unlikely to permit measurement of CNO neutrinos or of the ^{8}B spectral shape in the MSW transition region, it may offer sensitivity to the ^{8}B flux, first detection of *hep* neutrinos, and sensitivity to oscillation parameters via the day/night asymmetry (292).

6.6. Prospects

Figure 10 shows an overview of potential future measurements of the CNO neutrino flux. Since most of these experiments are in the proposal stage and are not yet funded, a degree of uncertainty exists in the projected detector capabilities and background levels. Two possible scenarios are shown in **Figure 10** for each project—a nominal and a stretch goal—and **Table 2** describes the assumptions for each data point. It is worth noting that the use of a 1.4% constraint on the *pep* flux follows the procedure adopted by the Borexino Collaboration in their CNO discovery paper (25), thus allowing for a like-for-like comparison. Full details of backgrounds and detector assumptions can be found in the relevant references.

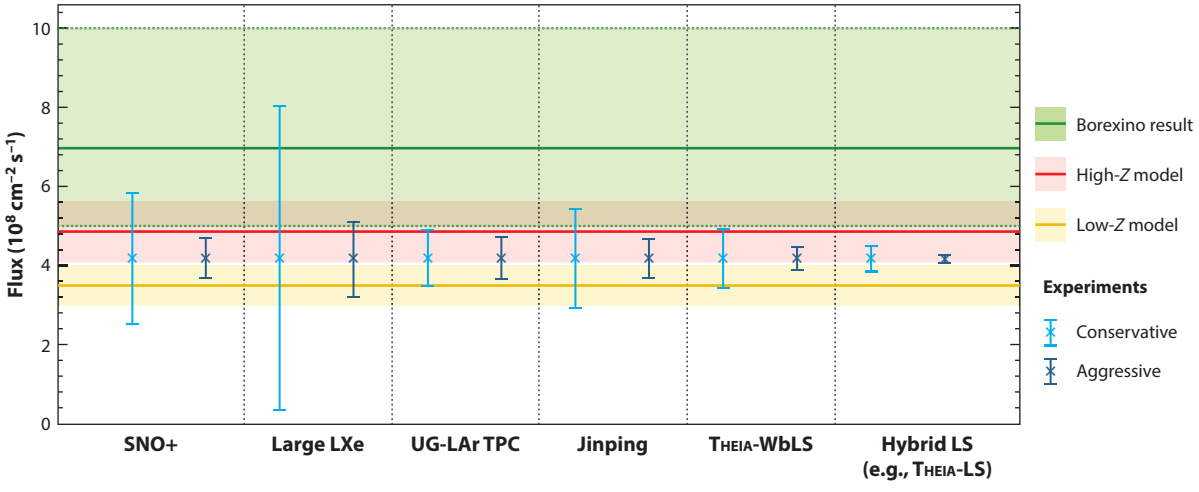

Figure 10

Prospects for measurement of the CNO neutrino flux, overlaid on the high-Z and low-Z model predictions, and the current observation from the Borexino experiment (25). Shaded bands represent uncertainties. Projected data points for each experiment are plotted at the midpoint between the high-Z and low-Z model predictions. Two data points for each experiment encompass a range of possible detector scenarios; in each pair, the left point (*light blue*) indicates the more conservative one (scenario 1), and the right point (*dark blue*) indicates the more aggressive one (scenario 2) (for details regarding these scenarios, see **Table 2**). Data from References 202, 252, 260, 262, 285, 288, and 293. Abbreviations: LS, liquid scintillator; LXe, liquid xenon; UG-LAr TPC, underground liquid argon time projection chamber; WbLS, water-based LS.

Table 2 Detector assumptions regarding potential future measurements of the CNO neutrino flux

Experiment	Scenario 1	Scenario 2
SNO+ (252)	5 years' exposure 1.4% *pep* constraint Current background levels	×10 reduction of ^{238}U and ^{232}Th ×1,000 reduction of ^{210}Bi
Large LXe (285)	200-tonne-year exposure 10^2 reduction of $2\nu\beta\beta$ 1% knowledge of backgrounds	2,000-tonne-year exposure 10^3 reduction of $2\nu\beta\beta$ Perfect knowledge of backgrounds
UG-LAr TPC (288)	400-tonne-year exposure 6,000 PEs per MeV, 0.6-MeV threshold Underground argon (negligible impact from ^{42}Ar, or pileup with ^{39}Ar) ^{222}Rn at 200 μBq per 100 t	^{222}Rn at 10 μBq per 100 t
Jinping (260)	1,500 days' exposure 1 kt fiducial 500 PEs per MeV	4 kt fiducial 1,000 PEs per MeV
THEIA-WbLS (202)	5 years' exposure 12.5 kt fiducial 55° angular resolution	60 kt fiducial 45° angular resolution
Hybrid LS (e.g., THEIA-LS) (262)	5 years' exposure 500 t fiducial Nanosecond-scale PMT TTS or 1.4% constraint on *pep*	25 kt fiducial 1.6 ns or better TTS No constraint on *pep*

The assumptions shown above are for more conservative (scenario 1) and more aggressive (scenario 2) projections regarding future measurements of the CNO neutrino flux (see **Figure 10**). Abbreviations: LS, liquid scintillator; LXe, liquid xenon; PE, photoelectron; PMT, photomultiplier tube; TTS, transit time spread; UG-LAr TPC, underground liquid argon time projection chamber; WbLS, water-based LS.

With no single-purpose detectors on the horizon, it seems likely that the future solar neutrino program will rely heavily on multipurpose detectors—from those designed for rare event searches to long-baseline neutrino experiments. Such detectors offer a wealth of potential opportunities on which we must capitalize to advance the field. The percent-level precision desirable for the *pp* flux may be most likely to come from the large noble liquid detectors planned for dark matter searches, given their low threshold, low intrinsic background, and good resolution. It would be interesting to be able to observe a larger number of *pp* neutrinos per day in real time, which would allow the observer to follow these measurements for a significant period and thereby study their long-term behavior with reasonable statistics. MeV-scale measurements—CNO and ^{8}B spectral measurements—may come from detectors designed primarily for NLDBD searches, such as large LS and hybrid detectors.

7. CONCLUDING REMARKS

While recent decades have offered tremendous advances in solar neutrinos across the fields of astrophysics, nuclear physics, and particle physics, many lingering mysteries remain.

The solar abundance problem remains open. Whether spectroscopic abundances, radiative opacity, or nonstandard modifications to solar models lie at its core remains to be seen. While progress is being made on all these fronts, independent measurements of solar abundances, ideally free from model dependencies, are needed. Solar neutrinos from the CNO cycle are a

unique opportunity in this regard and, in addition, offer a direct view on the pristine composition of our solar system. The Borexino experiment (25) has provided the first detection of these neutrinos, opening the road for future neutrino experiments. Given its size and depth, the SNO+ experiment could improve on the precision of the CNO neutrino flux measurement if sufficient background reduction can be achieved. Perhaps the best prospects for enhanced precision of future measurements beyond SNO+ lie in the concept of a hybrid detector that would offer directional sensitivity via Cherenkov detection in a low-threshold scintillation detector.

A precise measurement of *pp* neutrinos, another milestone for experimental solar neutrino physics, is needed to establish tight limits on the origin of the solar energy and set limits on nonstandard energy channels. The best prospects for such measurement may lie with multipurpose detectors: The low thresholds of liquid noble gas detectors, built for rare event searches, may yield excellent precision on *pp* neutrinos with sufficient control of background sources. Alternatively, large organic scintillator detectors may have good sensitivity given sufficiently low levels of ^{14}C.

Low-energy neutrinos are best addressed in large, low-threshold scintillator detectors. Precision measurements of the ^{7}Be and ^{8}B fluxes offer insights into the solar core temperature and nonstandard effects. A spectral measurement of ^{8}B neutrinos in the transition region between matter- and vacuum-dominated oscillation offers a unique chance to probe the details of the interaction of neutrinos with matter, with sensitivity to a range of potential nonstandard effects. At the other end of the solar neutrino spectrum, large water Cherenkov detectors (e.g., Hyper-K) and the DUNE LAr experiment offer the potential for significant observation of the day/night asymmetry, thus confirming the regeneration of electron-flavor neutrinos in the Earth at night and further constraining oscillation parameter values. A first measurement of *hep* neutrinos would complete the picture of solar neutrino fluxes. A precision measurement of Δm^2_{12} could resolve the current small tension between reactor and solar data. New data will come from SK+Gd, JUNO, SNO+, and other projects.

The nuclear reaction data for the Sun have yet to match the precision given by the ^{7}Be and ^{8}B neutrino fluxes. To address this imbalance, further experimental and theoretical efforts on nuclear reactions and a consolidated new evaluation of existing results are called for. The same is true for the CNO neutrino flux: The precision of the controlling CNO nuclear reaction data must be improved through the use of experiment, theory, and evaluations.

As more data are gathered and new experiments come online, the next decade may offer insights into several exciting open questions in this field with the potential to inform our understanding of solar evolution as well as neutrino properties.

SUMMARY POINTS

1. The solar abundance problem still awaits a solution.
2. Current solar neutrino fluxes favor a solar core with a temperature profile comparable to that seen in high-*Z* standard solar models, in agreement with helioseismic inferences of the solar sound speed and other helioseismic diagnostics.
3. A measurement of the flux of neutrinos from the CNO cycle allows a derivation of the total abundance of C and N in the solar core almost independently of solar model uncertainties.
4. Nuclear energy as the origin of solar luminosity is understood to a precision of 7% (1σ).

5. The nuclear reactions important for solar neutrinos have all been qualitatively identified, and their quantitative knowledge is precise to 5–20% depending on the reaction considered.
6. Neutrinos from all solar neutrino production branches have been observed except for the *hep* neutrinos.
7. The current knowledge of the electron survival probability curve allows room for physics beyond the Standard Model.
8. The future experimental program will likely rely on multipurpose detectors with broad programs.
9. The strongest solar neutrino program will leverage results from a wide range of experiments with complementary target materials, detection technology, and interaction types.

FUTURE ISSUES

1. Precise measurement of neutrinos from the CNO cycle would yield an independent indication of solar core composition. A 10% measurement would give results comparable in precision to those from spectroscopic techniques but almost free of model systematics.
2. Measurements of the electron neutrino survival probability in the energy region 2–5 MeV would be desirable to constrain and probe new physics.
3. Improved precision and additional real-time measurements of *pp* solar neutrinos would offer new opportunities to study the Sun.
4. Observation of *hep* neutrinos would add the final branch of the fusion chains to current measurements.
5. New laboratory and theoretical work is needed to improve the precision of solar fusion cross sections: for the *pp* chain $^{3}\mathrm{He}(\alpha, \gamma)^{7}\mathrm{Be}$ and $^{7}\mathrm{Be}(p, \gamma)^{8}\mathrm{B}$ to 3% and for the CNO cycle $^{14}\mathrm{N}(p, \gamma)^{15}\mathrm{O}$ to 5%.

DISCLOSURE STATEMENT

The authors are not aware of any affiliations, memberships, funding, or financial holdings that might be perceived as affecting the objectivity of this review.

ACKNOWLEDGMENTS

The authors wish to thank Wick Haxton for his expertise and numerous insights, and Steve Biller, Mark Chen, Josh Klein, Sean Paling, and Nigel Smith for fruitful discussions and input. Support is gratefully acknowledged from the following: in Germany, the Deutsche Forschungsgemeinschaft (BE 4100/4-1, ZU 123/21-1) and the COST Association (ChETEC, CA16117); in Spain, the Spanish Government through the MICINN grant PRPPID2019-108709GB-I00; and in the United States, the Director, Office of Science, of the US Department of Energy (contract DE-AC02-05CH11231), and the US Department of Energy, Office of Science, Office of Nuclear Physics (award DE-SC0018987).

LITERATURE CITED

1. Rutherford E, Soddy F. *London Edinburgh Dublin Philos. Mag. J. Sci.* 4:370 (1902)
2. von Weizsäcker CF. *Phys. Z.* 39:633 (1938)
3. Bethe HA. *Phys. Rev.* 55:103 (1939)
4. Vinyoles N, et al. *Astrophys. J.* 835:202 (2017)
5. Davis R, Harmer DS, Hoffman KC. *Phys. Rev. Lett.* 20:1205 (1968)
6. Cleveland BT, et al. *Astrophys. J.* 496:505 (1998)
7. Anselmann P, et al. *Phys. Lett. B* 285:376 (1992)
8. Hampel W, et al. *Phys. Lett. B* 447:127 (1999)
9. Kaether F, et al. *Phys. Lett. B* 685:47 (2010)
10. Altmann M, et al. *Phys. Lett. B* 616:174 (2005)
11. Abdurashitov JN, et al. *Phys. Rev. C* 80:015807 (2009)
12. Gavrin VN. The history, present and future of SAGE (Soviet-American Gallium Experiment). In *Solar Neutrinos: Proceedings of the 5th International Solar Neutrino Conference*, ed. M Meyer, K Zuber, pp. 29–46. Singapore: World Sci. (2019)
13. Hirata KS, et al. *Phys. Rev. Lett.* 63:16 (1989)
14. Fukuda Y, et al. *Phys. Rev. Lett.* 77:1683 (1996)
15. Abe K, et al. *Phys. Rev. D* 94:052010 (2016)
16. Wolfenstein L. *Phys. Rev. D* 17:2369 (1978)
17. Mikheyev SP, Smirnov AY. *Yad. Fiz.* 42:1441 (1985)
18. Chen HH. *Phys. Rev. Lett.* 55:1534 (1985)
19. Boger J, et al. *Nucl. Instrum. Methods Phys. Res. A* 449:172 (2000)
20. Ahmad Q, et al. *Phys. Rev. Lett.* 87:071301 (2001)
21. Ahmed SN, et al. *Phys. Rev. Lett.* 92:181301 (2004)
22. Alimonti G, et al. *Nucl. Instrum. Methods Phys. Res. A* 600:568 (2009)
23. Agostini M, et al. *Nature* 562:505 (2018)
24. Agostini M, et al. *Phys. Rev. D* 100:082004 (2019)
25. Agostini M, et al. *Nature* 587:577 (2020)
26. Eguchi K, et al. *Phys. Rev. Lett.* 90:021802 (2003)
27. Shibahashi H, Takata M. *Publ. Astron. Soc. Jpn.* 48:377 (1996)
28. Couvidat S, Turck-Chièze S, Kosovichev AG. *Astrophys. J.* 599:1434 (2003)
29. Buldgen G, et al. *Astron. Astrophys.* 621:A33 (2019)
30. Christensen-Dalsgaard J. *Rev. Mod. Phys.* 74:1073 (2002)
31. Aerts C, Christensen-Dalsgaard J, Kurtz DW. *Asteroseismology*. Dordrecht: Springer Neth. (2010)
32. Bahcall JN, Pinsonneault MH, Wasserburg GJ. *Rev. Mod. Phys.* 67:781 (1995)
33. Christensen-Dalsgaard J, et al. *Science* 272:1286 (1996)
34. Degl'Innoccenti S, Dziembowski WA, Fiorentini G, Ricci B. *Astropart. Phys.* 7:77 (1997)
35. Brun AS, Turck-Chièze S, Zahn JP. *Astrophys. J.* 525:1032 (1999)
36. Bahcall JN. *Phys. Rev. C* 65:025801 (2002)
37. Serenelli AM, Basu S, Ferguson JW, Asplund M. *Astrophys. J.* 705:L123 (2009)
38. Pinsonneault MH, Kawaler SD, Sofia S, Demarque P. *Astrophys. J.* 338:424 (1989)
39. Schlattl H, Weiss A. *Astron. Astrophys.* 347:272 (1999)
40. Turck-Chièze S, Palacios A, Marques JP, Nghiem PAP. *Astrophys. J.* 715:1539 (2010)
41. Guzik JA, Mussack K. *Astrophys. J.* 713:1108 (2010)
42. Zhang QS, Li Y, Christensen-Dalsgaard J. *Astrophys. J.* 881:103 (2019)
43. Christensen-Dalsgaard J. *Living Rev. Sol. Phys.* 18:2 (2021)
44. Asplund M. *Annu. Rev. Astron. Astrophys.* 43:481 (2005)
45. Asplund M, Grevesse N, Sauval AJ, Scott P. *Annu. Rev. Astron. Astrophys.* 47:481 (2009)
46. Bergemann M, Serenelli A. Solar abundance problem. In *Determination of Atmospheric Parameters of B-, A-, F- and G-Type Stars*, ed. E Niemczura, B Smalley, W Pych, pp. 245–58. Berlin: Springer (2014)
47. Lodders K. *Astrophys. J.* 591:1220 (2003)
48. Caffau E, et al. *Sol. Phys.* 268:255 (2011)

49. Lodders K, Palme H, Gail HP. Abundances of the elements in the Solar System. In *Landolt-Börnstein—Group VI Astronomy and Astrophysics*, Vol. 4B: *Solar System*, ed. JE Trümper. Berlin: Springer. **https://doi.org/10.1007/978-3-540-88055-4_34** (2009)
50. Grevesse N, Sauval AJ. *Space Sci. Rev.* 85:161 (1998)
51. Bahcall JN, Serenelli AM, Basu S. *Astrophys. J.* 621:L85 (2005)
52. Christensen-Dalsgaard J, di Mauro MP, Houdek G, Pijpers F. *Astron. Astrophys.* 494:205 (2009)
53. Bahcall JN, Serenelli AM, Pinsonneault M. *Astrophys. J.* 614:464 (2004)
54. Montalbán J, et al. Solar model with CNO revised abundances. In *Proceedings of SOHO 14: GONG 2004 Meeting: Helio- and Asteroseismology: Towards a Golden Future*, ed. D Danesy, p. 574. Paris: Eur. Space Agency (2004)
55. Antia HM, Basu S. *Astrophys. J.* 620:L129 (2005)
56. Delahaye F, Pinsonneault MH. *Astrophys. J.* 649:529 (2006)
57. Castro M, Vauclair S, Richard O. *Astron. Astrophys.* 463:755 (2007)
58. Basu S, Antia HM. *Phys. Rep.* 457:217 (2008)
59. Villante FL, Serenelli AM, Delahaye F, Pinsonneault MH. *Astrophys. J.* 787:13 (2014)
60. Song N, et al. *Mon. Not. R. Astron. Soc.* 477:1397 (2018)
61. Bahcall JN, Basu S, Serenelli AM. *Astrophys. J.* 631:1281 (2005)
62. Guzik JA. Reconciling the revised solar abundances with helioseismic constraints. In *Proceedings of SOHO 18/GONG 2006/HELAS I: Beyond the Spherical Sun*, ed. K Fletcher, M Thompson, CD-ROM, 17. Noordwijk, Neth.: ESA Publ. Div. (2006)
63. Haxton WC, Serenelli AM. *Astrophys. J.* 687:678 (2008)
64. Turck-Chièze S, Piau L, Couvidat S. *Astrophys. J.* 731:L29 (2011)
65. Serenelli AM, Haxton WC, Peña-Garay C. *Astrophys. J.* 743:24 (2011)
66. Basu S. *Living Rev. Sol. Phys.* 13:2 (2016)
67. Lin CH, Antia HM, Basu S. *Astrophys. J.* 668:603 (2007)
68. Vorontsov SV, Baturin VA, Ayukov SV, Gryaznov VK. *Mon. Not. R. Astron. Soc.* 430:1636 (2013)
69. Buldgen G, et al. *Mon. Not. R. Astron. Soc.* 472:751 (2017)
70. Serenelli A, Peña-Garay C, Haxton WC. *Phys. Rev. D* 87:043001 (2013)
71. Villante FL, Serenelli A. *Front. Astron. Space Sci.* 7:618356 (2021)
72. Bautista M, Hoppe R, Semenova E, Bergemann M. *Bull. AAS* 53(1). **https://baas.aas.org/pub/2021n1i142p01** (2021)
73. Cubas Armas M, Asensio Ramos A, Socas-Navarro H. *Astron. Astrophys.* 643:A142 (2020)
74. Iglesias CA, Rogers FJ. *Astrophys. J.* 464:943 (1996)
75. Badnell NR, et al. *Mon. Not. R. Astron. Soc.* 360:458 (2005)
76. Villante FL. *Astrophys. J.* 724:98 (2010)
77. Colgan J, et al. *Astrophys. J.* 817:116 (2016)
78. Blancard C, Cossé P, Faussurier G. *Astrophys. J.* 745:10 (2012)
79. Mondet G, Blancard C, Cossé P, Faussurier G. *Astrophys. J. Suppl. Ser.* 220:2 (2015)
80. Bailey JE, et al. *Nature* 517:56 (2015)
81. Nagayama T, et al. *Phys. Rev. Lett.* 122:235001 (2019)
82. Krief M, Feigel A, Gazit D. *Astrophys. J.* 821:45 (2016)
83. Krief M, Feigel A, Gazit D. *Astrophys. J.* 824:98 (2016)
84. Ovechkin AA, Loboda PA, Falkov AL. *High Energy Density Phys.* 30:29 (2019)
85. Hoarty DJ, et al. *High Energy Density Phys.* 32:70 (2019)
86. Perry TS, et al. *High Energy Density Phys.* 35:100728 (2020)
87. Nahar SN, Pradhan AK. *Phys. Rev. Lett.* 116:235003 (2016)
88. More RM, Hansen SB, Nagayama T. *High Energy Density Phys.* 24:44 (2017)
89. Krief M, Kurzweil Y, Feigel A, Gazit D. *Astrophys. J.* 856:135 (2018)
90. Baggott RA, Rose SJ, Mangles SPD. *Phys. Rev. Lett.* 125:145002 (2020)
91. Thoul AA, Bahcall JN, Loeb A. *Astrophys. J.* 421:828 (1994)
92. Serenelli A. *Eur. Phys. J. A* 52:78 (2016)
93. Adelberger EG, et al. *Rev. Mod. Phys.* 70:1265 (1998)

94. Adelberger EG, et al. *Rev. Mod. Phys.* 83:195 (2011)
95. Bahcall JN, Serenelli AM, Basu S. *Astrophys. J. Suppl. Ser.* 165:400 (2006)
96. Burbidge EM, Burbidge GR, Fowler WA, Hoyle F. *Rev. Mod. Phys.* 29:547 (1957)
97. Casella C, et al. *Nucl. Phys. A* 706:203 (2002)
98. Mossa V, et al. *Nature* 587:210 (2020)
99. Broggini C, Bemmerer D, Guglielmetti A, Menegazzo R. *Annu. Rev. Nucl. Part. Sci.* 60:53 (2010)
100. Broggini C, Bemmerer D, Caciolli A, Trezzi D. *Prog. Part. Nucl. Phys.* 98:55 (2018)
101. Bemmerer D, et al. The new Felsenkeller 5 MV underground accelerator. In *Solar Neutrinos: Proceedings of the 5th International Solar Neutrino Conference*, ed. M Meyer, K Zuber, pp. 249–63. Singapore: World Sci. (2019)
102. Lane AM, Thomas RG. *Rev. Mod. Phys.* 30:257 (1958)
103. Descouvemont P, Baye D. *Rep. Prog. Phys.* 73:036301 (2010)
104. Marcucci LE, Mangano G, Kievsky A, Viviani M. *Phys. Rev. Lett.* 116:102501 (2016)
105. Neff T. *Phys. Rev. Lett.* 106:042502 (2011)
106. Dohet-Eraly J, et al. *Phys. Lett. B* 757:430 (2016)
107. Vorabbi M, Navrátil P, Quaglioni S, Hupin G. *Phys. Rev. C* 100:024304 (2019)
108. Assenbaum HJ, Langanke K, Rolfs C. *Z. Phys. A* 327:461 (1987)
109. Salpeter EE. *Aust. J. Phys.* 7:373 (1954)
110. Raiola F, et al. *Eur. Phys. J. A* 19:283 (2004)
111. Huke A, et al. *Phys. Rev. C* 78:015803 (2008)
112. Cvetinovic A, Lipoglavsek M, Markelj S, Vesic J. *Phys. Rev. C* 92:065801 (2015)
113. Zylstra AB, et al. *Phys. Rev. C* 101:042802 (2020)
114. Gruzinov AV, Bahcall JN. *Astrophys. J.* 490:437 (1997)
115. Savage MJ, et al. *Phys. Rev. Lett.* 119:062002 (2017)
116. Bonetti R, et al. *Phys. Rev. Lett.* 82:5205 (1999)
117. Holmgren HD, Johnston RL. *Phys. Rev.* 113:1556 (1959)
118. Bemmerer D, et al. *Phys. Rev. Lett.* 97:122502 (2006)
119. deBoer RJ, et al. *Phys. Rev. C* 87:015802 (2013)
120. Szücs T, et al. *Phys. Rev. C* 99:055804 (2019)
121. Zhang X, Nollett KM, Phillips DR. *J. Phys. G* 47:054002 (2020)
122. Junghans AR, et al. *Phys. Rev. Lett.* 88:041101 (2002)
123. Junghans AR, et al. *Phys. Rev. C* 81:012801 (2010)
124. Buompane R, et al. *Eur. Phys. J. A* 54:92 (2018)
125. Bemmerer D, et al. *J. Phys. G* 36:045202 (2009)
126. Leblanc PJ, et al. *Phys. Rev. C* 82:055804 (2010)
127. Bruno CG, et al. *Phys. Rev. Lett.* 117:142502 (2016)
128. Li Q, et al. *Phys. Rev. C* 93:055806 (2016)
129. Wagner L, et al. *Phys. Rev. C* 97:015801 (2018)
130. Bertone PF, et al. *Phys. Rev. Lett.* 87:152501 (2001)
131. Angulo C, Descouvemont P. *Nucl. Phys. A* 690:755 (2001)
132. Formicola A, et al. *Phys. Lett. B* 591:61 (2004)
133. Imbriani G, et al. *Eur. Phys. J. A* 25:455 (2005)
134. Runkle RC, et al. *Phys. Rev. Lett.* 94:082503 (2005)
135. Marta M, et al. *Phys. Rev. C* 78:022802 (2008)
136. Marta M, et al. *Phys. Rev. C* 83:045804 (2011)
137. Daigle S, et al. *Phys. Rev. C* 94:025803 (2016)
138. Angulo C, et al. *Nucl. Phys. A* 656:3 (1999)
139. Rolfs C, Azuma RE. *Nucl. Phys. A* 227:291 (1974)
140. Schröder U, et al. *Nucl. Phys. A* 467:240 (1987)
141. Mohr P, Iliadis C. *Nucl. Instrum. Methods Phys. Res. A* 688:62 (2012)
142. Epelbaum E, et al. *Phys. Rev. Lett.* 112:102501 (2014)
143. Bahcall JN. *Phys. Rev. D* 41:2964 (1990)

144. Stonehill LC, Formaggio JA, Robertson RG. *Phys. Rev. C* 69:015801 (2004)
145. Villante FL. *Phys. Lett. B* 742:279 (2015)
146. Fogli GL, Lisi E, Marrone A, Palazzo A. *Phys. Lett. B* 583:149 (2004)
147. Bahcall JN, Gonzalez-Garcia MC, Peña-Garay C. *J. High Energy Phys.* 0408:016 (2004)
148. Arpesella C, et al. *Phys. Rev. Lett.* 101:091302 (2008)
149. Gonzalez-Garcia MC, Maltoni M, Salvado J. *J. High Energy Phys.* 1005:72 (2010)
150. Bergström J, et al. *J. High Energy Phys.* 1603:132 (2016)
151. Vinyoles N, et al. *J. Cosmol. Astropart. Phys.* 1510:015 (2015)
152. Vinyoles N, Vogel H. *J. Cosmol. Astropart. Phys.* 1603:002 (2016)
153. Vescovi D, et al. *J. Phys. G* 48:015201 (2021)
154. Bahcall JN, May RM. *Astrophys. J.* 155:501 (1969)
155. Bellini G, et al. *Nature* 512:383 (2014)
156. Esteban I, et al. *J. High Energy Phys.* 1701:87 (2017)
157. Esteban I, et al. *J. High Energy Phys.* 2009:178 (2020)
158. Serenelli AM. *Astrophys. Space Sci.* 328:13 (2010)
159. Gough DO. *Mon. Not. R. Astron. Soc.* 485:L114 (2019)
160. Agostini M, et al. *Eur. Phys. J. C* 80:1091 (2020)
161. Wuchterl G, Klessen RS. *Astrophys. J.* 560:L185 (2001)
162. Izotov YI, Thuan TX. *Astrophys. J.* 710:L67 (2010)
163. Maki Z, Nakagawa M, Sakata S. *Prog. Theor. Phys.* 28:870 (1962)
164. Mikheyev SP, Smirnov AY. *Nuovo Cim. C* 9:17 (1986)
165. Wolfenstein L. *Phys. Rev. D* 17:2369 (1978)
166. Bethe HA. *Phys. Rev. Lett.* 56:1305 (1986)
167. Haxton WC. *Phys. Rev. Lett.* 57:1271 (1986)
168. Parke SJ. *Phys. Rev. Lett.* 57:1275 (1986)
169. Agarwalla SK, et al. *J. High Energy Phys.* 2002:38 (2020)
170. Abe K, et al. arXiv:1805.04163 [physics.ins-det] (2018)
171. de Gouvêa A, Martinez-Soler I. *Phys. Lett. B* 809:135751 (2020)
172. Aharmim B, et al. *Phys. Rev. D* 72:052010 (2005)
173. Aharmim B, et al. *Phys. Rev. D* 102:062006 (2020)
174. Bergmann S, Grossman Y. *Phys. Rev. D* 59:093005 (1999)
175. Friedland A, Lunardini C, Peña-Garay C. *Phys. Lett. B* 594:347 (2004)
176. Ohlsson T. *Rep. Prog. Phys.* 76:044201 (2013)
177. Bakhti P, Rajaee M. *Phys. Rev. D* 102:035024 (2020)
178. Giarnetti A, Meloni D. arXiv:2005.10272 [hep-ph] (2020)
179. Dutta B, et al. *J. High Energy Phys.* 2009:106 (2020)
180. Aharmim B, et al. *Phys. Rev. D* 70:093014 (2004)
181. Abe K, et al. arXiv:2012.03807 [hep-ex] (2020)
182. Bellini G, et al. *Phys. Lett. B* 696:191 (2011)
183. Malaney RA, Meyer BS, Butler MN. *Astrophys. J.* 352:767 (1990)
184. Hostert M, Pospelov M. arXiv:2012.02142 [hep-ph] (2020)
185. Fargion D. *J. High Energy Phys.* 0406:045 (2004)
186. de Holanda PC, Smirnov AY. *Phys. Rev. D* 83:113011 (2011)
187. Diaz A, et al. *Phys. Rep.* 884:1 (2020)
188. Lee BW, Shrock RE. *Phys. Rev. D* 16:1444 (1977)
189. Agostini M, et al. *Phys. Rev. D* 96:091103 (2017)
190. Beacom JF, Bell NF. *Phys. Rev. D* 65:113009 (2002)
191. Barenboim G, et al. *J. Cosmol. Astropart. Phys.* 2103:087 (2021)
192. Graham PW, et al. *Annu. Rev. Nucl. Part. Sci.* 65:485 (2015)
193. Sikivie P. *Rev. Mod. Phys.* 93:015004 (2021)
194. Raffelt GG, Dearborn DSP. *Phys. Rev. D* 36:2211 (1987)
195. Raffelt GG. *Phys. Rep.* 198:1 (1990)

196. Marsh DJE. *Phys. Rep.* 643:1 (2016)
197. Schlattl H, Weiss A, Raffelt G. *Astropart. Phys.* 10:353 (1999)
198. Capozzi F, Raffelt G. *Phys. Rev. D* 102:083007 (2020)
199. Arceo Díaz S, et al. arXiv:1910.10568 [astro-ph.SR] (2019)
200. Kubodera K, Nozawa S. *Int. J. Mod. Phys. E* 3:101 (1994)
201. Bahcall JN. *Rev. Mod. Phys.* 50:881 (1978)
202. Askins M, et al. *Eur. Phys. J. C* 80:416 (2020)
203. Bahcall JN. *Phys. Rev. C* 56:3391 (1997)
204. Bahcall JN, et al. *Phys. Rev. C* 54:411 (1996)
205. Alonso J, et al. arXiv:1409.5864 [physics.ins-det] (2014)
206. Kostensalo J, Suhonen J, Giunti C, Srivastava PC. *Phys. Lett. B* 795:542 (2019)
207. Pavićević MK, et al. *Nucl. Instrum. Methods Phys. Res. A* 895:62 (2018)
208. Kostensalo J, Suhonen J, Zuber K. *Phys. Rev. C* 101:031302 (2020)
209. Wolfsberg K, et al. The molybdenum solar neutrino experiment. In *Solar Neutrinos and Neutrino Astronomy*, ed. ML Cherry, K Lande, WA Fowler, pp. 196–202. New York: Am. Inst. Phys. (1985)
210. Yeh M, et al. *Nucl. Instrum. Methods Phys. Res. A* 660:51 (2011)
211. Bignell L, et al. *J. Instrum.* 10:P12009 (2015)
212. So SH, et al. *Adv. High Energy Phys.* 2014:327184 (2014)
213. Onken DR, et al. *Mater. Adv.* 2020(1):71 (2020)
214. Guo Z, et al. *Astropart. Phys.* 109:33 (2019)
215. Biller SD, Leming EJ, Paton JL. *Nucl. Instrum. Methods Phys. Res. A* 972:164106 (2020)
216. Lyashenko A, et al. *Nucl. Instrum. Methods Phys. Res. A* 958:162834 (2020)
217. Kaptanoglu T, et al. *Phys. Rev. D* 101:072002 (2020)
218. Li M, et al. *Nucl. Instrum. Methods Phys. Res. A* 830:303 (2016)
219. Caravaca J, Land B, Yeh M, Orebi Gann G. *Eur. Phys. J. C* 80:867 (2020)
220. Caravaca J, et al. *Eur. Phys. J. C* 77:811 (2017)
221. Caravaca J, et al. *Phys. Rev. C* 95:055801 (2017)
222. Gruszko J, et al. *J. Instrum.* 14:P02005 (2019)
223. Dalmasson J, et al. *Phys. Rev. D* 97:052006 (2018)
224. Dunger J, Biller SD. *Nucl. Instrum. Methods Phys. Res. A* 943:162420 (2019)
225. Aberle C, et al. *J. Instrum.* 9:P06012 (2014)
226. Wonsak B, et al. *J. Instrum.* 13:P07005 (2018)
227. Jiang R, Elagin A. arXiv:1902.06912 [physics.ins-det] (2019)
228. Li A, et al. *Nucl. Instrum. Methods Phys. Res. A* 947:162604 (2019)
229. Lebanowski L, et al. *Nucl. Instrum. Methods Phys. Res. A* 890:133 (2018)
230. Graham E, et al. *J. Instrum.* 14:P11024 (2019)
231. Buck C, Yeh M. *J. Phys. G* 43:093001 (2016)
232. Zuber K. *Phys. Lett. B* 571:148 (2003)
233. Zuber K. *Phys. Lett. B* 709:6 (2012)
234. Cribier M. (LENS Collab.) *Nucl. Phys. B Proc. Suppl.* 87:195 (2000)
235. Fukuda S, et al. *Phys. Rev. Lett.* 86:5651 (2001)
236. Aharmim B, et al. *Phys. Rev. C* 81:055504 (2010)
237. Aharmim B, et al. *Phys. Rev. C* 88:025501 (2013)
238. Renshaw A, et al. *Phys. Rev. Lett.* 112:091805 (2014)
239. Ahmad Q, et al. *Phys. Rev. Lett.* 89:011302 (2002)
240. Aharmim B, et al. *Phys. Rev. D* 98:112013 (2018)
241. Aharmim B, et al. *Phys. Rev. D* 99:032013 (2019)
242. Beacom JF, Vagins MR. *Phys. Rev. Lett.* 93:171101 (2004)
243. Takeuchi Y. *Nucl. Instrum. Methods Phys. Res. A* 952:161634 (2020)
244. Bellini G, et al. *Phys. Rev. Lett.* 108:051302 (2012)
245. Bellini G, et al. *Phys. Rev. Lett.* 107:141302 (2011)
246. Bellini G, et al. *Phys. Rev. D* 89:112007 (2014)

247. Abe S, et al. *Phys. Rev. C* 84:035804 (2011)
248. Gando A, et al. *Phys. Rev. C* 92:055808 (2015)
249. Gando A, et al. *Phys. Rev. Lett.* 117:082503 (2016). Addendum. *Phys. Rev. Lett.* 117:109903 (2016)
250. Gando A, et al. *Phys. Rev. Lett.* 122:192501 (2019)
251. Anderson M, et al. *J. Instrum.* 16:P05009 (2021)
252. Andringa S, et al. *Adv. High Energy Phys.* 2016:6194250 (2016)
253. Anderson M, et al. *Phys. Rev. D* 99:012012 (2019)
254. An F, et al. *J. Phys. G* 43:030401 (2016)
255. Djurcic Z, et al. arXiv:1508.07166 [physics.ins-det] (2015)
256. Bellini G, et al. *Phys. Rev. D* 82:033006 (2010)
257. Abusleme A, et al. arXiv:2006.11760 [hep-ex] (2020)
258. Cheng JP, et al. *Annu. Rev. Nucl. Part. Sci.* 67:231 (2017)
259. Guo Z, et al. *Chin. Phys. C* 45:025001 (2021)
260. Beacom JF, et al. *Chin. Phys. C* 41:023002 (2017)
261. Bonventre R, Orebi Gann G. *Eur. Phys. J. C* 78:435 (2018)
262. Land B, et al. *Phys. Rev. D* 103:052004 (2021)
263. Seo SH. arXiv:1903.05368 [physics.ins-det] (2019)
264. Freedman DZ. *Phys. Rev. D* 9:1389 (1974)
265. Drukier A, Stodolsky L. *Phys. Rev. D* 30:2295 (1984)
266. Cabrera B, Krauss LM, Wilczek F. *Phys. Rev. Lett.* 55:25 (1985)
267. Akimov D, et al. *Science* 357:1123 (2017)
268. Akimov D, et al. *Phys. Rev. Lett.* 126:012002 (2021)
269. Dutta B, Strigari LE. *Annu. Rev. Nucl. Part. Sci.* 69:137 (2019)
270. Billard J, Strigari LE, Figueroa-Feliciano E. *Phys. Rev. D* 91:095023 (2015)
271. Agnese R, et al. *Phys. Rev. D* 95:082002 (2017)
272. Strauss R, et al. *Eur. Phys. J. C* 77:506 (2017)
273. Strigari LE. *Phys. Rev. D* 93:103534 (2016)
274. Dutta B, Liao S, Strigari LE, Walker JW. *Phys. Lett. B* 773:242 (2017)
275. Coloma P, Esteban I, Gonzalez-Garcia M, Maltoni M. *J. High Energy Phys.* 2002:23 (2020). Addendum. *J. High Energy Phys.* 2012:71 (2020)
276. Coloma P, Gonzalez-Garcia M, Maltoni M, Schwetz T. *Phys. Rev. D* 96:115007 (2017)
277. Coloma P, et al. *J. High Energy Phys.* 1704:116 (2017)
278. Denton PB, Gehrlein J. *J. High Energy Phys.* 2104:266 (2021)
279. Denton PB, Farzan Y, Shoemaker IM. *J. High Energy Phys.* 1807:37 (2018)
280. Aprile E, et al. *Phys. Rev. Lett.* 126:091301 (2021)
281. Cerdeño DG, et al. *J. High Energy Phys.* 1605:118 (2016). Erratum. *J. High Energy Phys.* 1609:48 (2016)
282. Aalbers J, et al. *J. Cosmol. Astropart. Phys.* 1611:017 (2016)
283. Aalbers J, et al. *Eur. Phys. J. C* 80:1133 (2020)
284. Kostensalo J, Suhonen J, Zuber K. arXiv:2009.01164 [nucl-th] (2020)
285. Newstead JL, Strigari LE, Lang RF. *Phys. Rev. D* 99:043006 (2019)
286. Agnes P, et al. *Phys. Rev. D* 93:081101 (2016)
287. Cattadori CM. *J. Phys. Conf. Ser.* 375:042008 (2012)
288. Franco D, et al. *J. Cosmol. Astropart. Phys.* 1608:017 (2016)
289. Haselschwardt S, Lenardo B, Pirinen P, Suhonen J. *Phys. Rev. D* 102:072009 (2020)
290. Acciarri R, et al. arXiv:1601.02984 [physics.ins-det] (2016)
291. Kostensalo J, Suhonen J, Zuber K. *Phys. Rev. C* 97:034309 (2018)
292. Capozzi F, Li SW, Zhu G, Beacom JF. *Phys. Rev. Lett.* 123:131803 (2019)
293. Cerdeño DG, Davis JH, Fairbairn M, Vincent AC. *J. Cosmol. Astropart. Phys.* 1804:037 (2018)